2012 TDEM Final Report: Starshade Stray Light Mitigation through Edge Scatter Modeling and Sharp Edge Materials Development

Rev B, 5/4/2016

Suzanne Casement (PI), Steven Warwick, Daniel Smith, Onur Armagan
Northrop Grumman Corporation
Redondo Beach, CA 90278

JPL Document #1533541

Approvals

Approved/ _____   ___5/17/16___

Suzanne Casement   Date
Principal Investigator, Northrop Grumman

Approved/ _____   _____

Nick Siegler   Date
Exoplanet Exploration Program Chief Technologist, JPL

Approved/ _____   _____

Douglas Hudgins   Date
Exoplanet Exploration Program Scientist, NASA HQ

Revision Record:

REVISION	DATE	REVISION/CHANGE DESCRIPTION	SECTIONS AFFECTED
--	3/4/2016	Initial submission to the TAC	--
A	4/13/2016	Revision based on TAC comments	All
B	5/4/2016	Revision based on TAC review	Primarily: 1.1, 4.2, 4.4, all of 5, 6.1, plus miscellaneous typos and grammar edits

CONTENTS

1 EXECUTIVE SUMMARY

A key goal expressed by the Astro2010 Decadal Survey for exoplanet exploration is to develop a mission that is capable of directly detecting and spectrally characterizing potentially habitable exoplanets[1]. Achieving this groundbreaking science requires an optical system capable of observing a planet as faint as 4×10^{-11} the brightness of its host star with as little as 0.065 arcsecond (") separation from that star[2]. The light from the star must be almost completely suppressed so that it doesn't overwhelm the light from the planet. Starshades, external occulting screens that block starlight before it enters the telescope, are a leading candidate for this anticipated exoplanet direct-detection mission[1].

To achieve the required level of suppression performance, any stray light source on the starshade must be carefully controlled so that it doesn't overwhelm the exoplanet signal. This is one of the critical technologies for the starshade architecture and is therefore an important area of focus for our technology development efforts. Stray light is considered to be any light that scatters from or transmits through the starshade structure. This includes sunlight and starlight transmission through the starshade membrane, as well as sunlight or other background light scattering from the structure in the direction of the telescope[3]. Sources of stray light have been studied in previous starshade development activities and the design of the starshade structure mitigates their effects[4,5].

Of the stray light sources considered, the largest after controlling the target star diffraction is the scattering of sunlight off of the edge of the starshade and into the telescope. This scattered light source is mitigated to a large degree by the distance between the starshade and the telescope (30,000 to 80,000 km, depending on the mission design) and by operating the system with only the edge of the starshade visible to both the telescope and the sun (Figure 1-1).
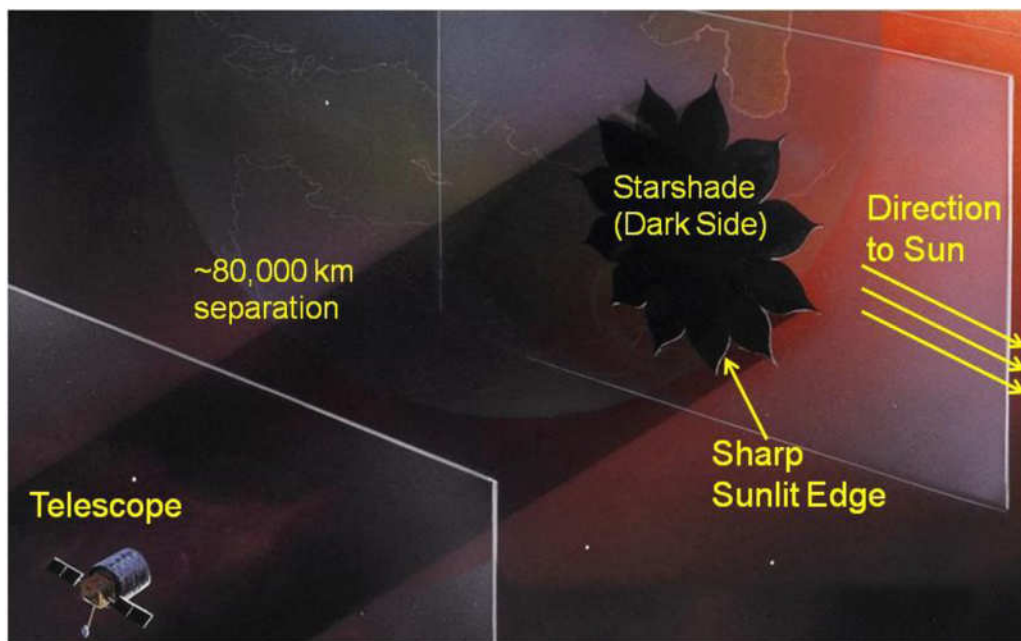

Figure 1-1: A depiction of the on-orbit starshade system. The sharp optical edge of the starshade is the only sunlit area that is visible to the telescope. The telescope-facing side of the starshade is kept out of the sunlight during observing. The sharpness and scattering properties of the edge determine the amount of solar scattered light entering the telescope.

The primary influence on the level of scattered light that does enter the telescope via edge scatter is the detailed configuration of the starshade edge (its sharpness and scattering properties). Therefore, the requirement to limit scattered light in the telescope[3] translates into stringent requirements on the properties of the starshade edge. The amount of scattered light can be minimized by making the area of the edge very small. Given that there is a large edge length along all of the petals, this means that the width (i.e. radius of curvature, RoC) of the edge must be very small. Additionally, the scattered light from the edge is minimized by making it non-reflective (typically black) and controlling the direction in which the light scatters. Here, we present the results of our model and test campaign to understand how the detailed surface properties of the starshade edge material, including coatings, interact with the complex shape of the edge to determine the overall edge scattering properties. We discuss the impact of our findings on the design and architecture of a flight system to detect and characterize earth-like exoplanets, including recommendations for design / manufacturing objectives in future technology development programs.

1.1 MILESTONE COMPLIANCE

Under this TDEM we have made significant progress towards TRL 4, advancing our knowledge of sharp edge properties through both laboratory measurements and simulation.

Our TDEM milestone (Sections 2.2 and 6.1) is comprised of development of a new stray light model and the fabrication and measurement of sharp-edge test coupons. The stray light model we developed allows us to simulate the full starshade edge with the scatter properties of any measured material. The model is limited to simple geometrical raytracing, but provides detailed insight into the image plane distribution of the scattered light. These data allow us to compare the predicted brightness of the edge with the expected brightness of exoplanets (Figure 1-2). These comparisons are the first means by which to quantify the exoplanet detectability of various edge designs and can be utilized to derive design requirements. These results can then be incorporated into an image simulation of the planet, star
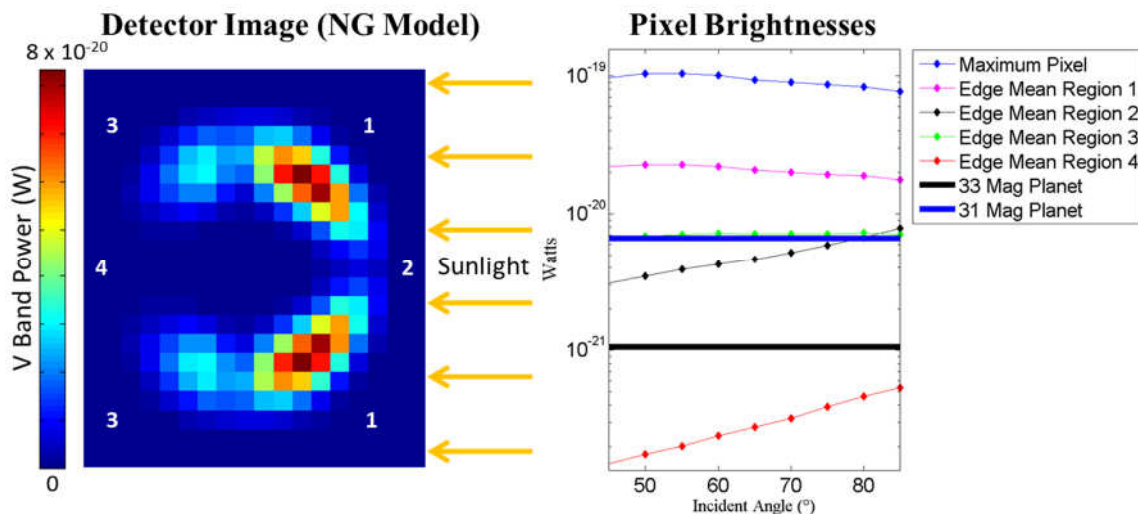

Figure 1-2: Milestone Goal – Develop a stray light simulation. The simulation developed enables us to model the on-orbit performance of a wide variety of edge concepts. Simulation results for a Titanium substrate coated with an Acktar Magic Black ™ coating with a 20 μm edge RoC. Plot at the left is for a 75° incidence angle while right shows the relative brightness at all modeled incidence angles for the 4 defined regions. The predicted stray light is compared to the brightness of a 31st and 33rd magnitude planet as median and faintest planets expected to be detectable[2].

(leakage), telescope, and detector properties to determine an effective inner working angle (IWA) at which planets can be detected for a given signal to noise ratio, observation time, planet / star brightness, or any other set of parameters one could choose to evaluate. The model also showed linear dependence between the light scattered and the edge RoC, allowing simple scaling of results.

The second part of our TDEM milestone requires the fabrication and laboratory measurements of at least two sharp edge test samples. We constructed samples of four potential starshade edge concepts and completed laboratory measurements of the edge scatter properties for each. Lab measurements were compared to a simplified version of the model to establish its validity. Some configurations showed very poor correlation to the predictions, but these were regions of very poor ray sampling statistics. The shapes of the curves were reasonably correlated for all measurements, but absolute values were under predicted by at least 3x and in some cases > 10x

Figure 1-3: Milestone Goal – Build and test sharp edge samples. At left is a photograph of the sample and at right is a Scanning Electron Microscope (SEM) image of the sample edge. Four samples made of different materials were built and tested. Their scatter properties were also input into the model to assess their on-orbit performance.

even when there were good ray statistics. Several factors contribute to the differences, but the largest is likely fabrication variation of the samples which will be shown in Section 4.3.4 to contribute ~ 2x variation, possibly more in some cases. Additional variation may be due to differences between estimated and actual RoC as the 20 μm value used in the model is estimated by eye for the samples. Further discussion is in Section 5.3.2.
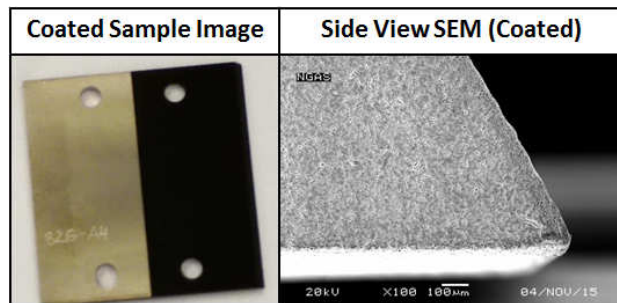
The results of the 2012 Edge Scatter TDEM are encouraging. This work provides information for both the development of a mission architecture that can be supported by available edge performance today, and identifies a likely performance level the edge can achieve for scattered light with some additional engineering design work. The as-modeled edge scatter for the NWO architecture was below the planet brightness in some areas and even in the brightest areas was only 2-4x brighter. Additional allocation for edge variation and model uncertainty factors due to the good qualitative but poor numerical agreement between the model and the measurements suggests this approach is perhaps 10x brighter than needed for this architecture to meet the ExoPlanet Detection and Characterization objectives, including margin. Potential approaches could be different scatter properties (specular) and better (smaller, less variable) RoC. These data may be used in a larger architecture study to address the key mission requirements.

Overall our results give insight into the starshade edge design required to meet the mission objectives. They ground our model in reality and the manufacture/measurement of the sharp edge samples and their on-orbit performance assessment given by the model serves as a step towards the design and fabrication of edge materials to flight-like requirements. The model outputs provide an opportunity to assess the detectability of exoplanets using a variety of edge configurations and provide information for developing realistic and balanced requirements for the starshade system to meeting this very challenging technical problem.

4

2 KEY TDEM DETAILS

2.1 OBJECTIVE

An external occulter mission, or starshade, is one of the methods being studied for the detection and characterization of extra-solar planets around nearby stars. Several teams are studying the requirements for such a mission and identifying the technical challenges that must be addressed if the mission were to be undertaken. In the Exoplanet Exploration Programs (ExEP) Technology Plan Appendix, control of stray light remains a primary technical challenge facing a starshade-based mission[3].

To be sure that stray light in the starshade system will not overwhelm a predicted planet signal of ~31 – 33* magnitudes[2], all contributors of stray light into the telescope must be evaluated. One source of stray light is from the parent star leaking past the starshade; this is addressed by the design and construction of the starshade and is the focus of other technology development efforts. A second contribution is from the sunlight that scatters from the edge of the starshade. Because of the geometry of the system, only the very edge of the starshade is visible to both the sun and the telescope (Figure 2-1). Since the starshade is 10s of meters in diameter, however, the illuminated edge can still add up to a significant area. Understanding the options to control sunlight scattering from this edge, through a combination of making the edge narrow and making it black, and deriving a methodology to develop requirements for the starshade edge design in order to meet the stray light requirements of a flight system, is the focus of this TDEM.

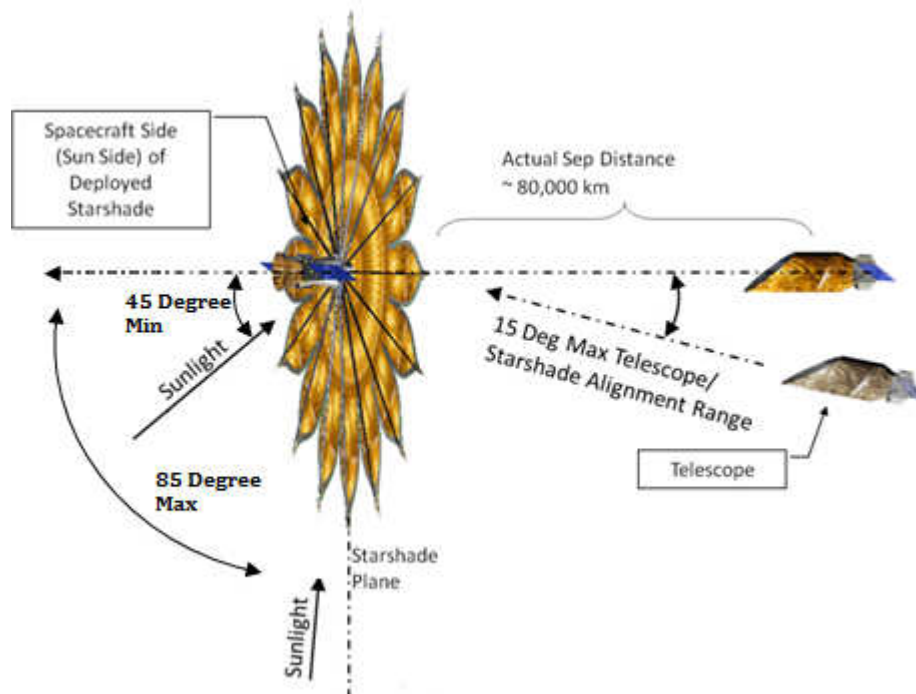**Figure 2-1:** The geometry of the starshade system, emphasizing the requirements of telescope/sun orientation relative to the starshade. Geometric restraints to the system ensure that only the edge of the starshade is visible to both the sun and the telescope.

* Calculated using $m_p - m_* = 26$ magnitudes and Figure 10b of [2] which shows a median target of $m_* = 5$ mag and an extreme of $m_* \sim 7$ mag

In support of NASA's ExEP and the Technology Development for Exoplanet Missions (TDEM) component of NASA's strategic Astrophysics Technology (SAT) solicitation, this final report presents the results of our research and demonstrates compliance to our TDEM milestone (Section 2.3). The results presented in this report are consistent with the scope of the proposal submitted in March, 2013[6] and the White Paper for this TDEM approved by the TAC in December, 2014.

2.2   TDEM MILESTONE AND TECHNOLOGY READINESS LEVEL (TRL) ASSESSMENT

Prior to the work of this TDEM, the progress towards meeting the overall mission scattered light control requirements had reached TRL 3 for the primary source of stray light: scattering from the sunlit edges of the starshade. This TRL 3 assessment is based on previous internal development at Northrop Grumman (NG), in which we evaluated the design options put forth in the New Worlds Observer (NWO) Astrophysics Strategic Mission Concept Study (ASMCS)[4] via a stray light model developed in TracePro[7,8]. Table 2-1 below shows our initially proposed research goals to bring the starshade edge technology from TRL 3 to TRL 6.

Goal	Exit Criteria	TRL
Develop design concept; use analytical scattered light model to evaluate design options	Analytical studies demonstrate design objectives achievable. Results documented	3
Fabricate sample of starshade edge and test	Demonstrate edge RoC requirements that are within current state of the art for manufacturing	3+
Measure BRDF of flight-like options and incorporate into system model	Demonstrate low fidelity laboratory model that meets the edge RoC and scattered light predictions, tested in laboratory conditions	4
Perform thermal and structural analysis of the edge composition and construction	Demonstrate structural and dimensional stability to required level in error budget via model	5
Build one section of edge structure to flight requirements	Demonstrate required scale fabrication process	5+
Perform full flight qualification for material properties and measure scatter performance after environmental exposure	Demonstrate on subscale (high fidelity) model the ability to meet requirements after environmental exposure	6

Table 2-1: Research goals proposed to bring starshade edge technology to TRL 6. The first goal had already been achieved under NG internal funds but was updated as part of this TDEM. Goals highlighted in green are needed to achieve TRL 4 and were addressed in this TDEM effort. The remaining goals are required to achieve TRL 6 for the overall starshade edge scattered light control.

Our objective for this study is to further our understanding of the edge requirements of the starshade and to develop the edge treatment technology, raising it from TRL 3 to TRL 4 by addressing the goals in the highlighted rows (in green) in Table 2-1. Our milestone to drive this effort is:

TDEM Milestone: Develop a scattered light simulation and use it to derive requirements for the edge radius of curvature and scattering properties; build and test at least two sharp edge samples to evaluate the feasibility of flight-compatible materials being fabricated to the derived requirements and how well such a sample performs compared to the predictions of the simulation.

The modeling work done under this TDEM provides a comprehensive physical model, utilizing a detailed CAD model of the starshade as the input. Measured scatter properties of our proposed materials are used as inputs for the edge properties. A system level model is used to predict performance and is described in Section 5.

Coupons were fabricated that demonstrate that an edge RoC of ~15 µm is achievable using standard fabrication techniques in some materials, with Titanium showing the best results. The coatings chosen added very little to the RoC, though handling did ding the corners on several samples. Flat Bi-directional Reflectance Distribution Function (BRDF, defined in Section 4.2) measurements were made on the coupons and were used to characterize the starshade edge in the scatter model, which output detector flux distributions to be compared with the flux of a notional planet.

The objectives of TRL 4 have largely been met by successfully fabricating sharp edge samples (Section 3), measuring their scatter in the laboratory (Section 4), and scaling the results by the starshade edge geometry (Section 5). We have developed a methodology that can be exploited for the testing of various materials, coatings, and mission configurations to develop detailed requirements towards a flight design. There are still some discrepancies between the measurements and model predictions have must be resolved to definitively achieve TRL 4. These were discovered late and the resolution was not achievable within the available resources of this TDEM. However, our results do provide significant progress by supplying key information for the maturation of a starshade mission architecture, and also identify additional steps to take to further develop the control of scattered sunlight.

2.3 TDEM TIMELINE

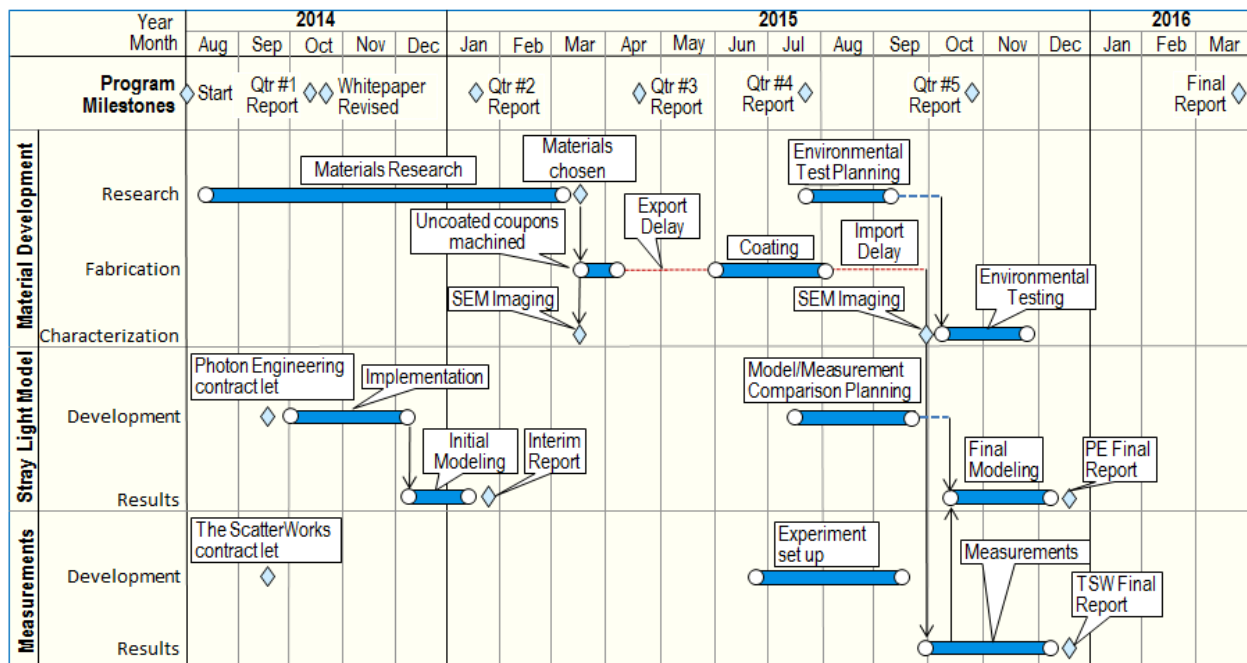Figure 2-2 shows the as-executed schedule of activities on this TDEM.

Figure 2-2: Timeline of TDEM activities

The differences from the initial proposed timeline[6] are primarily due to a delay in the initial white paper review and longer than expected import/export compliance related delays that took place while dealing with the foreign suppliers who performed the surface treatments on our test samples. These delays extended our period of performance into CY16.

3 MATERIAL SELECTION AND FABRICATION

A key aspect of our TDEM milestone is to develop sharp edge samples of at least two starshade edge concepts.

In order to build the test samples we had to first evaluate, based on the available published data, the optical and mechanical properties of the potential edge materials and identify the best candidates for testing[9]. The surface treatment selection process is documented in Section 3.1.1, and the substrate selection process is documented in Section 3.1.2. Section 3.2 characterizes the design and fabrication of the sharp edge samples.

3.1 CANDIDATE MATERIAL PROPERTIES AND SELECTION

3.1.1 SURFACE TREATMENT (COATING) SELECTION AND CHARACTERIZATION

Seven potential surface treatments were identified that warranted further analysis. Each surface treatment was ranked based on its optical performance (blackness), durability (adherence and response to thermal loads), suitability to edges (thickness), substrate versatility, and flight readiness. These five categories provide a comprehensive evaluation of the parameters relevant to the selection of a material for flight. A starshade must minimize the scattered light into the telescope from all sources. The best way to achieve this is to have an edge coating that is extremely black, and thus highly absorptive in the solar band. Just as important to flight performance is that the edge holds its shape, which requires the coating to be highly thermally conductive and have a high emissivity in order to transfer heat efficiently and to avoid thermal distortions. Thermal properties of the coatings are also of interest because of the large variation in incident radiation on the different parts of the starshade edge, resulting from the likely rotation of the starshade during integration and the many possible orientations of the starshade relative to the sun. These considerations are the basis of our *optical performance* and *durability* categories of analysis (see Figure 3-1). To minimize the area of sunlit edge visible to the telescope, our analysis favors thinner coatings in order to drive the edge RoC down (the *suitability to edges* category). Materials already indicated to be suitable to space environments are favored as they have the highest probability for future flight qualification (*flight readiness* category). Finally, for experimental ease and the desired applicability of our results to various mission architectures, coatings suitable to a variety of substrates are favored (*substrate versatility* category). For each category the coatings were scored (green for high performance, yellow for average performance, or red for poor performance) and the scores were then weighted by the categories relevance to design goals and combined into an overall suitability score.

The seven surface treatments considered were Acktar Magic Black™, Enbio CoBlast SolarBlack™, vertically-aligned Carbon NanoTubes (VA-CNT), multi-walled Carbon NanoTubes (MW-CNT), N-Science Deep Space Black™, Avian-EP Black™, and black Silicon. Figure 3-1 below summarizes the results of our analysis of the suitability of each candidate coating to our TDEM effort.

Coating:		Acktar	Enbio	VA-CNT	MW-CNT	N-Science	Avian	Silicon
Analysis Parameter	**Weight**							
Reflectivity	10							
Durability	8							
Substrate versatility	6							
Edge Suitability	4							
Flight Readiness	2							
Suitability Score:		46	46	36	36	18	14	24

Figure 3-1: A summary of the suitability assessment of various surface treatments. Green/yellow/red corresponds to high/medium/poor performance, respectively. Grey boxes indicate that information was not found at the time of assessment. Green rankings scored 2, yellow scored 1, and red scored -1. Scores were then multiplied by the category weight to calculate the overall suitability score (bottom).

After our analysis was complete, the data compiled was used to downselect from seven candidate coatings to two. Carbon NanoTubes (CNT) showed the best optical performance (Total Integrated Scatter < 0.1% on a Silicon substrate), but due to the cost and schedule required to build these, and because they ranked lower than two other candidates in our suitability criteria (due to their fragility and the large dependence of the optical performance on the substrate), we elected to not include them in this study. A follow-up study that could include samples of CNT would be highly desirable given their optical performance. Instead, we selected **Acktar Magic Black™** and **Enbio CoBlast SolarBlack™** as our surface treatments. These two coatings ranked highest in the suitability criteria, mainly due to their proven durability and extreme versatility to various substrates. Though not the best of the candidates considered, their reflectivity is comparable to that of the others except for the CNTs, where it is an order of magnitude worse.

	Acktar	Enbio
TIS (%, Vis)	< 2 (typically)	< 5
Thickness (µm)	4 - 6	2 - 5
Solar Absorption (.2 - 2.5 µm)	Not Known	> 0.93
Emissivity (%)	> 93	> 70
Substrates	Ti, Al, BeCu	Ti, Al, Cu, Mg, SS, Inconel
Conductivity	Not Known	Not Known
Working T (K)	4 - 623	120 - 820

Table 3-1: Key parameters of the Acktar Magic Black™ and Enbio CoBlast SolarBlack™ coatings, taken from vendors' websites and published materials. They were not measured by NG.

Enbio's SolarBlack™ coating was developed for the European Space Agency as a coating for the heatshield of the Solar Orbiter satellite. It is a thin, black, ceramic coating deposited using Enbio's proprietary CoBlast technique (see link in References for more information on Enbio), which involves removing the oxide layer of the substrate, roughening its surface, and applying the coating[10]. The key features of SolarBlack™ that resulted in its selection are its thinness, high Solar absorptance and emissivity, low Total Integrated Scatter (TIS), and the testing completed deeming it qualified for use on the Solar Orbiter (see Table 3-1)[10]. Acktar's Magic Black™ surface treatment is an inorganic thin black coating deposited via a proprietary physical vapor deposition method[11]. The key features of Magic Black™ that resulted in its selection are its thinness, thermal properties, adherence to a diverse range of substrates, low TIS, and testing completed deeming it qualified for use on the METIS coronagraph, also on the Solar Orbiter mission (see Table 3-1)[11,12].

3.1.2 SUBSTRATE SELECTION

The selection of the substrates to be fabricated into sharp edge coupons was based on previous NG thermal analyses of the starshade structure. Our approach assumes a rigid edge can be accommodated by the deployment scheme as with the ASMCS deployment methodology. Other deployment schemes, such as the one assumed for the Exo-S architecture[13], require the edge to be flexible for deployment.

We chose to include a BeCu substrate (alloy 17200) because it has been proposed as a potential tip material for the Hypergaussian starshade. Using Electrical Discharge Machining (EDM) methods we have demonstrated the ability to fabricate a tip with the approximate characteristics required for a minimal truncation of the Hypergaussian shape.

We chose Titanium as a substrate because it is a material often selected for spacecraft structure due to its high stiffness to weight ratio and its low thermal conductivity. It is also a very common material for coating and was identified as a coating substrate by both Acktar and Enbio, unlike the BeCu. We believed that Titanium's stiffness would make it machinable into a much sharper edge than other substrate materials we considered which was somewhat borne out in the results.

Finally, we chose Aluminum as a "proof of concept" substrate material given its ease of manufacture and ease of coating for nearly all coating processes. This proved ideal, as Enbio was unable to coat the BeCu substrates without significant non-recurring engineering (NRE) costs and schedule extensions.

Although we did not include flexible materials in our study, we expect that it may be possible to fabricate BeCu in a thin enough sheet to meet both the edge geometry (Section 3.2) and flexibility requirements that would satisfy the Exo-S highly flexible edge requirement with appropriate fabrication and handling techniques. Titanium is a less clear option for a deployment scheme requiring flexible materials, but other materials with similar thermal and mechanical properties (e.g. some steel alloys) may also be ideal candidates for the coatings we tested under this study. Future work could be done to demonstrate the flexibility of our selected edge materials. As the deployment scheme matures, other metals that meet its requirements should be analyzed as potential materials for the starshade edge.

3.2 TEST COUPON DESIGN AND CHARACTERIZATION

Our baseline was to fabricate a set of flat test coupons and test them before a sharp edge coupon was designed[6]. However, most of that data was found in the literature and so we elected to move directly to fabrication of sharp edge samples.

Figure 3-2 shows the general flight architecture of the starshade edge and a diagram of what a sharp edge sample looks like relative to this design. The samples have straight edges, built as close to flight like as possible, with an edge length of 5 cm to allow ease of handling and fabrication. This also means that they are sufficiently oversized compared to the 3 mm beam size of the lasers in the lab measurement setup (see Section 4), which avoids any effects from the end of the sample in our measurements.

We fabricated multiple samples from all three selected substrates. The samples were shaped via an EDM process using facilities at NG. After fabrication, the samples were imaged with a Scanning Electron Microscope (SEM), the edge RoC was estimated, and they were then sent out to Acktar and Enbio for coating. The minimum coating requirement given to the vendors is represented by the blue shading in Figure 3-2, and ensured that enough of the samples were coated for standard scattering properties to be measured from the sample flat as well as the edge (see Section 4.2). Two Al samples, four Ti samples, and four BeCu samples were coated by Acktar. Four Al samples and four Ti samples were coated by Enbio. Unfortunately Enbio was unable to coat the BeCu substrates without significant NRE costs and extended schedule. Upon return, SEM images were taken of the coated samples to determine the effect that coating had on the edge.

Figure 3-2: The general architecture of the starshade petal construction and edge detail is shown in the top figure. The design of our sharp edge test coupons shown in the bottom figure is a great simplification of the flight design to provide ease of fabrication for these tests.

This fabrication process resulted in four substrate-coating combinations to be tested experimentally (Section 4): Acktar-Ti, Acktar-BeCu, Enbio-Al, and Enbio-Ti. As detailed in Section 3.1.2, the Aluminum substrate was initially included in our materials selection as it was very inexpensive to manufacture and most coatings are designed to work with it. The Aluminum samples were only to be used in testing if the BeCu or Titanium samples could not be used. Therefore, we did not test the Acktar-Al sample.

A characterization of each sharp edge sample to be tested is given in Figures 3-3, 3-4, 3-5, and 3-6. Each figure contains SEM images of the coupon edge before and after coating, a photograph of the coated coupon, and the RoC of the edge before and after coating. The RoC of the coated edge of each sample is approximately 20 μm.
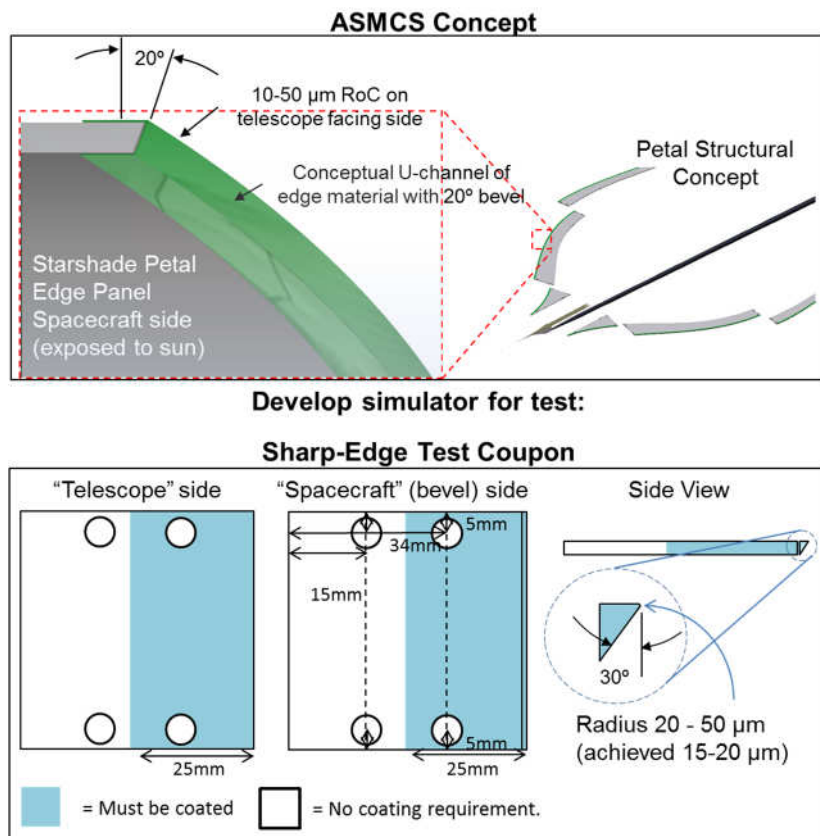
Acktar-Ti

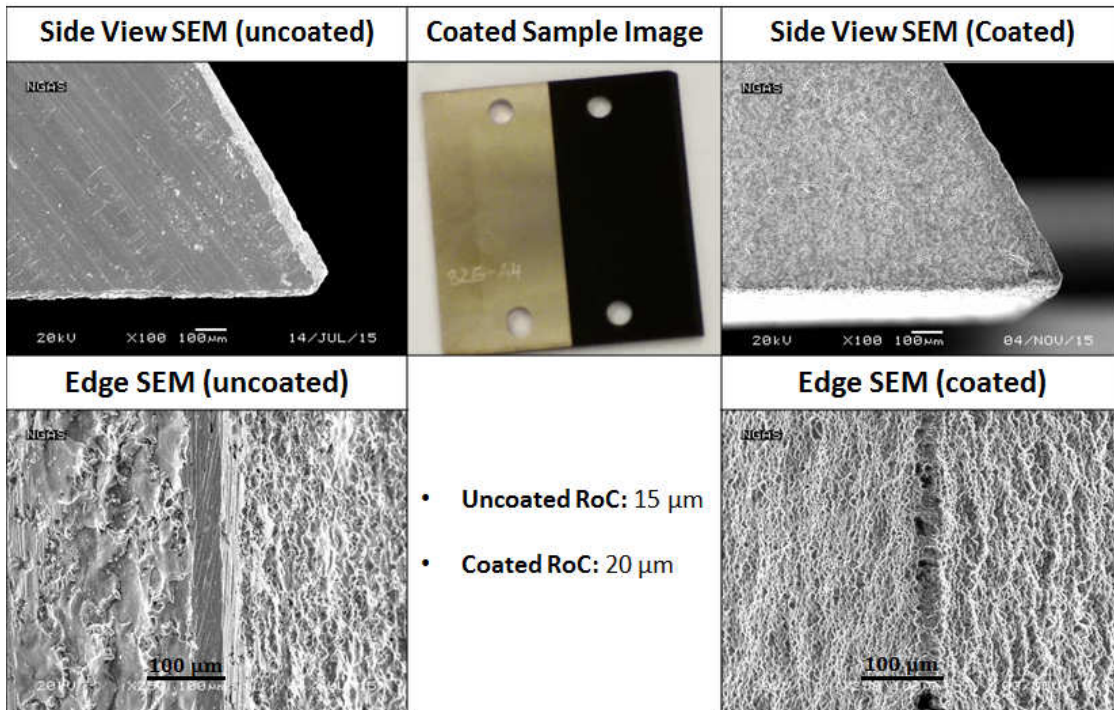| Side View SEM (uncoated)	Coated Sample Image	Side View SEM (Coated)
Edge SEM (uncoated)		**Edge SEM (coated)**
	• **Uncoated RoC:** 15 μm • **Coated RoC:** 20 μm	

Figure 3-3: Titanium sharp edge coupon coated with Acktar Magic Black™. On these and subsequent images, the top two SEMs are looking down the edge from the side. In these, the left figure is slightly tilted such that the face of the bevel is slightly exposed on the right side of the image. On the right, the sample is tilted so the bottom is slightly exposed. The out of focus faces are seen as brighter in the image. The lower two SEMs are looking down at the edge itself. The location of the two images is not correlated.
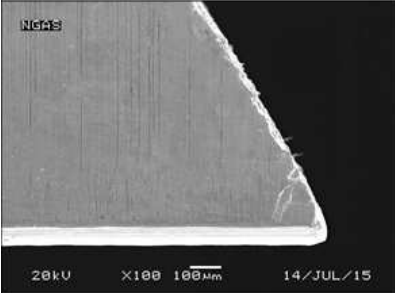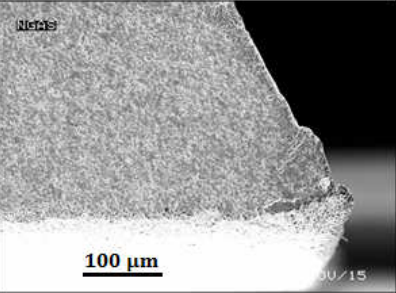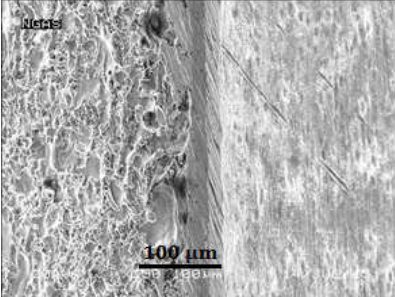
Acktar-BeCu

Figure 3-4: Beryllium-Copper sharp edge coupon coated with Acktar Magic Black™. The sample is quite tilted in the coated edge image on the upper right and the corner appears damaged, making it difficult to estimate the RoC.

Enbio-Al

Figure 3-5: Aluminum sharp edge coupon coated with Enbio CoBlast SolarBlack™. As above, the upper right image is highly tilted showing the bottom of the sample.
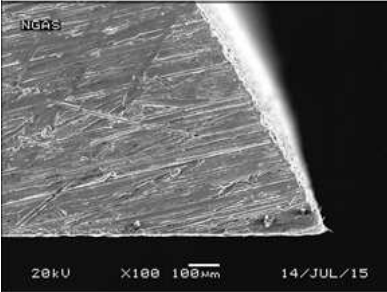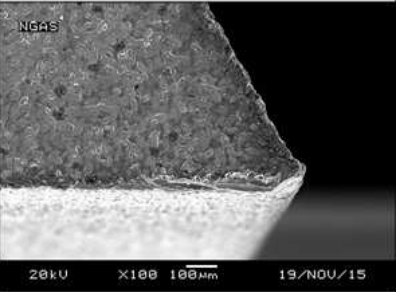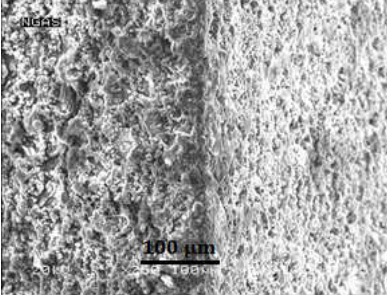
Enbio-Ti
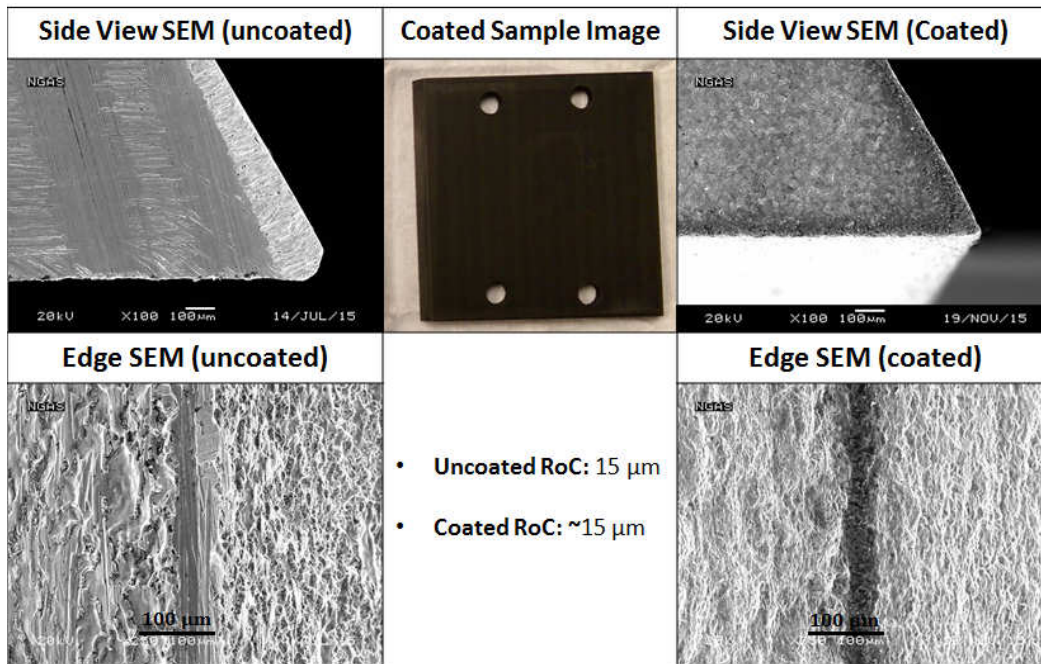
Figure 3-6: Titanium sharp edge coupon coated with Enbio CoBlast SolarBlack™. While the upper right shows a large tilt, exposing the bottom of the sample, it also shows a near perfect corner, likely the sharpest of all the samples measured.

3.3 ENVIRONMENTAL TESTING

To evaluate the durability of the flight materials during ground handling, launch, and in the on-orbit environment, significant environmental testing must be done to qualify the selected materials and processes. Though not directly identified as a task in our TDEM milestone, we conducted an initial assessment of our coating and substrate selections to evaluate their potential as an approach for flight, including a post-environmental assessment of their optical performance. As a full and rigorous environmental test sequence was not within the scope of this TDEM, only a subset of relevant environmental tests was performed. A test sequence was established based on an evaluation of the environmental testing requirements that apply to coatings. The procedures leverage heavily off of the James Webb Space Telescope membrane TRL 6 development and the relevant MIL Standards (810 G, 1540 C, 1540 D, 343).

The subset of tests we performed were a tape adhesion test, cyclic abrasion test, thermal cycling test, and humidity exposure test. The parameters and results of each test are detailed in the subsections below. Table 3-2 summarizes the tests performed on each sample.

Coupon Number	Substrate	Coating	Testing Completed
0000825-A1	Aluminum	Acktar	Cyclic Abrasion, Tape Adhesion
0000826-A1	Titanium	Acktar	Cyclic Abrasion, Tape Adhesion
0000826-A2	Titanium	Acktar	Tape Adh., T/C, Humidity Exp., Post Exp. Tape Adh., Optical[1]
0000827-A1	BeCu	Acktar	Cyclic Abrasion, Tape Adhesion
0000827-A3	BeCu	Acktar	Tape Adh., T/C, Humidity Exp., Post Exp. Tape Adh., Optical[1]
0000825-B2	Aluminum	Enbio	Tape Adh., T/C, Humidity Exp., Post Exp. Tape Adh., Optical[1]
0000825-C1	Aluminum	Enbio	Cyclic Abrasion, Tape Adhesion
0000826-B2	Titanium	Enbio	Tape Adh., T/C, Humidity Exp., Post Exp. Tape Adh., Optical[1]
0000826-B3	Titanium	Enbio	Cyclic Abrasion, Tape Adhesion

Table 3-2: Summary of the environmental tests performed on each of 9 test coupons.
[1]The optical tests performed on the post-test coupons are documented in Section 4.4.

3.3.1 TEST DESCRIPTIONS

Cyclic abrasion testing was performed in order to simulate the possible edge abrasion conditions occurring during launch vibrations and as a general test of durability. Kapton film was determined to be the most likely material over which the starshade edges would interface with and was therefore used during testing. For these tests specifically, clean 3-mil Kapton HN was used as the abrasion substrate. The 2"x 2" coated coupons were placed into a fiberglass mount so that the coated flat of the samples lined up with the abrasion surface. The fixture was then weighted to apply the predetermined test loads. Coupons were manually cycled 100 times at 0.3 psi, visually examined for degradation and subsequently tested for an additional 50 cycles loaded at 1.0 psi. Photographs representative of this process are shown below in Figure 3-7.
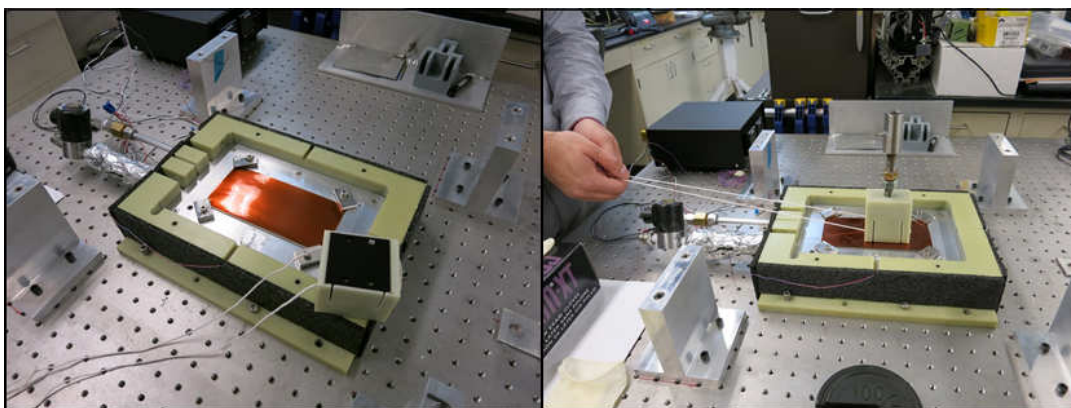
Figure 3-7: NG cyclic abrasion test setup. The Kapton HN abrasion surface lies flat and the mounted sample lies on top and is cycled manually.

Thermal cycling from 100K to 400K (-280° F to 260° F) for a total of six cycles over 13 hours, followed by exposure to 75% relative humidity at 330K (135° F) for 226 hours, was done per MIL-STD to gauge low level ground testing and storage survivability of the candidate materials. The temperature range was set by estimating the on-orbit environment. Testing was conducted in a thermal laboratory at NG. Visual inspection and a tape adhesion test were performed on the coupons following test completion.

The procedure for tape adhesion testing was derived from an internal process document used for the application of vapor-deposited Aluminum (VDA) due to the similar nature of the candidate coating processes to the VDA case. Coating adhesion was tested on each sample by applying and removing a 1-

15

inch wide 3M No. 250 adhesive tape to the sample flat. Certain exceptions to the process document procedure relating to quantity and distance from surface edges were taken due to the size of the test coupons. These adhesion tests were performed on the samples before and after thermal cycling/humidity exposure and also after cyclic abrasion (see Table 3-2). The tape test does not relate to any particular I&T process, but instead is being used as a generic indication of the comparative adhesion properties of the two coatings.

3.3.2   TEST RESULTS

Our results indicated no performance dependence on the substrate, so we report results for each of the two coatings without distinguishing which substrate they are adhered to.

The initial pristine (pre-thermal/humidity testing) sample adhesion test results are shown in Figure 3-8. The tape test was completed twice, once in each direction, to test for sensitivity to directionality. The Acktar coating demonstrated no noticeable coating removal; the Enbio coatings show significant coating removal, which may be

Figure 3-8: Tape adhesion test results for a subset of the pristine samples coated by Acktar (left) and Enbio (right). Significant residue on tape was observed for all EnBio samples.

indicative of an inferior application process or binder system. Both coating processes are proprietary which makes it difficult to compare the systems rigorously. Application via a vapor deposition process (Acktar) generally yields a hard and durable coating. Since the CoBlast deposition process (Enbio) is a complete unknown, however, not even a speculative comparison between the techniques can be made.

Results of the cyclic abrasion tests were documented visually, both photographically (Figure 3-9) and through SEM (not included). In addition to visual examination, tape adhesion testing was completed post abrasion to detect any underlying weakness in the coatings caused

Figure 3-9: Visual inspection of the Acktar (left) and Enbio (right) coupons after cyclic abrasion testing. Particulate from the Kapton is apparent, but there is no observed damage to the coupon coatings.

by the physical abrasion process (Figure 3-10).

Visual examination was completed after 100 cycles at 0.3 psi and after 50 cycles at 1.0 psi. The results were consistent, showing no discernable difference between the midway and final points. As seen in

16

Figure 3-9, the majority of the abrasive damage occurred to the Kapton substrate, leaving yellow particulate matter on the surface of the coupons. We expect any particulate material from the Kapton to be cleaned off the edge surfaces as a final I&T step prior to launch. Any abrasion and particulate matter caused by launch dynamics can be mitigated using a Starshade stow technique which does not bring the Kapton into close proximity with the coated edges.

During subsequent tape adhesion testing (Figure 3-10), the coating removal remained consistent with pre-test adhesion results (Figure 3-8); no removal of the Acktar coating was observed but there was still significant removal of the Enbio coating. Kapton particulate from the coupon surface was removed in both cases. SEM results on the cycled coupons revealed little damage to the coupon edge, but did show coating removal on the corners. It is hard to determine the exact cause of this damage, but the

Figure 3-10: Adhesion test results after cyclic abrasion testing for the Acktar (left) and Enbio (right) coupons. Both the Kapton surface used for abrasion (copper colored material) and the tape are shown.

location and lack of damage on the remainder of the edge points towards coupon handling as the cause rather than damage caused during testing. The SEM images of all 5 coupons, containing both edge-on and side views, are not included in this report but are available upon request.

The thermal cycling and humidity exposure test results were evaluated through visual examination, tape adhesion testing, and SEM imagery. Monitoring of the thermal lab during testing confirm that the coupons were exposed to the exact thermal cycles and humidity conditions described in Section 3.3.1. Visual examination (Figure 3-11) yielded no discernable difference between the coupons pre- and post-exposure. Results of the tape adhesion testing (Figure 3-12) were similar to the previous tests completed after initial coating and cyclic abrasion testing: the Acktar coating demonstrated no noticeable coating removal while portions of the Enbio coatings removed readily.

Figure 3-11: Visual inspections of the Acktar (left) and Enbio (right) coupons after thermal cycling and humidity exposure. No effects were observed.

Based on the results, a clear distinction can be made between the Acktar Magic Black™ and Enbio CoBlast SolarBlack™ coating systems with regards to material durability. Based solely on these environmental tests performed, omitting the post-testing optical performance measurements (Section 4.4) and pre-existing environmental testing of both coatings, it seems that the Acktar coating has a significant advantage over the Enbio coating. Though both coatings survived cyclic abrasion and environmental exposure based on visual inspection, the Enbio coating continually failed tape adhesion testing.

With regards to substrate compatibility, both coatings demonstrate the ability to maintain a desired edge RoC after coating, but once again the Enbio coatings are inferior with regards to adhesion. Failed coating adhesion can be cause for concern regarding both contamination control as well as long term optical performance. Though a more rigorous sequence of environmental testing is undoubtedly required for all potential starshade edge materials, these initial test results should be kept in mind moving forward.

Figure 3-12: Adhesion test results after thermal cycling/humidity exposure for the Acktar (bottom) and Enbio (top) coupons.

4   STRAY LIGHT MEASUREMENTS

To satisfy the measurement aspect of our TDEM milestone, we engaged with The ScatterWorks (TSW), recognized as experts in the field of scatter measurements, to measure the scatter properties of the sharp edge samples detailed in Section 3. The measurements taken and their relevance to achieving our milestone are outlined in Table 4-1:

Measurement	Purpose	Milestone Relevance
Flat Surface BRDF	Measure optical properties for implementation into the stray light model. Leads to model prediction of on-orbit edge performance for each candidate material.	On-orbit performance predictions needed to derive edge RoC requirements for each candidate material.
Sharp-Edge Scatter Measurement	Directly measure scatter properties of sample edges. Yields experimental predictions to compare to model results.	Experimental setup to be run in stray light model and compared to measurements to establish ground truth.

Table 4-1: The two categories of measurements performed by TSW, their purpose within our TDEM effort, and their relevance to our TDEM milestone. Each measurement has its own subsection below. See Section 4.2 for a definition of BRDF.

This section presents the measurements summarized in Table 4-1, as well as details regarding the experimental setup.

4.1   THE SCATTERWORKS LAB SETUP

An image of the TSW lab is shown in Figure 4-1. The lab uses a CASI (Complete Angle Scatter Instrument) scatterometer to make its measurements. CASI is a scatterometer that measures scattered light in sweeps along the incident plane, sweeping straight through the specular beam rather than blocking it from the measurement. Sweeps through various orientations by CASI are automated with a large degree of angular accuracy and precision. For more information on t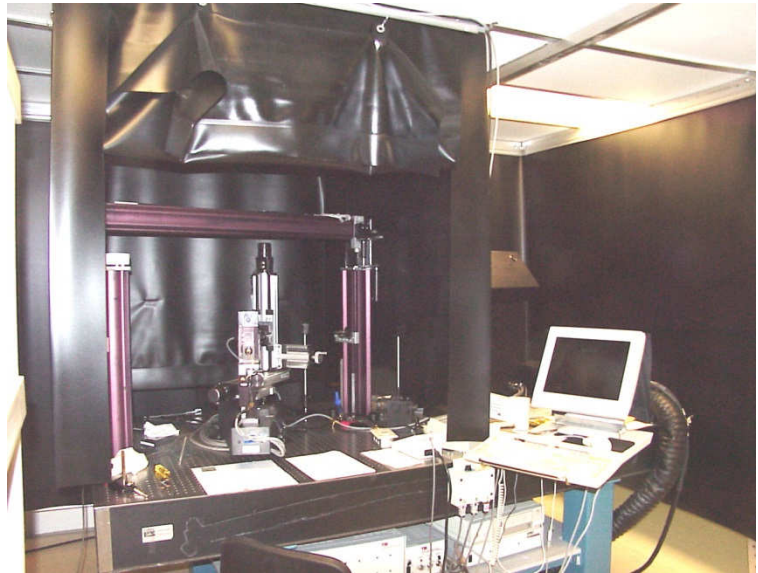he CASI instrument, see the link in the References Section. Measurements were made at wavelengths of 633 nm and 488 nm. Both lasers were circularly polarized so the test sample would

Figure 4-1: TSW lab setup.

receive equal amounts of S and P light for all sample orientations, just as it would from sunlight. The lab is set up under high-efficiency particulate arresting (HEPA) filters to assure a flow of clean air, and the optical table is surrounded by a black curtain to reduce any contaminating signal, resulting in a detector-limited noise floor of ~10^{-8} (BRDF units, sr^{-1}). Separation between the scatter surface (the sharp edge of the sample) and the detector is about 30 cm. The detector subtends an angle of 0.00178 steradians.

4.2   FLAT SURFACE BRDF MEASUREMENTS
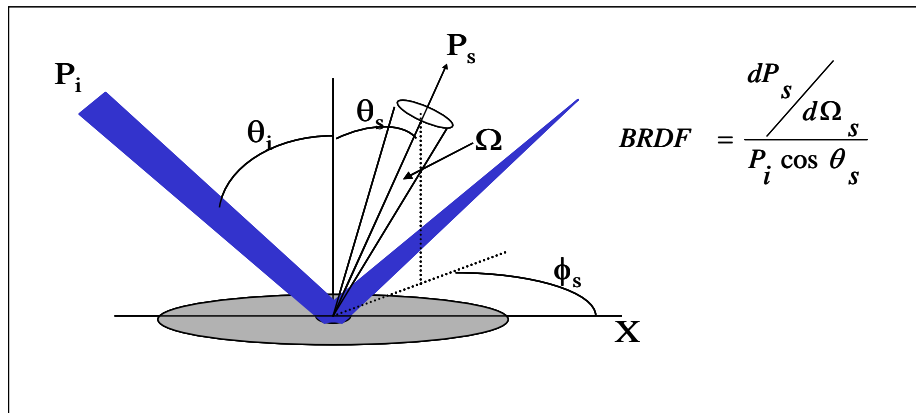
Figure 4-2: Mathematical definition and diagram of the relevant parameters of BRDF.

In order to characterize how the on-orbit starshade edge will perform when made from each of our candidate substrate/coating combinations, the optical properties of each test sample had to be provided as an input to the stray light model (see Section 5). The optical properties of each sample were delivered to the model by measuring their Bidirectional Reflectance Distribution Function, or BRDF.

BRDF is a function of four variables: two angles describing the direction of the light scattered from a surface (θ_s and ϕ_s, seen in Figure 4-2) and two angles describing the direction of the incident beam (θ_i, seen in Figure 4-2. ϕ_i is not diagramed, but is analogous to ϕ_s for the incident beam). The BRDF value is the ratio of scattered power in a particular direction (θ_s, ϕ_s), through a solid angle Ω, to the power

19

Acktar-BeCu Flat-Surface BRDF

Legend:
- $\theta_i = 5°$
- $\theta_i = 38°$
- $\theta_i = 55°$
- $\theta_i = 68°$
- $\theta_i = 80°$

Y-axis: BRDF (sr^{-1})
X-axis: Scatter Angle (θ_s, Degrees)

Figure 4-3: BRDF measured by TSW for the Acktar-BeCu sharp edge sample. The specular reflection is minimized by the Lambertian properties of the diffuse coating which pushes the scatter into the plane of the material, realized as the "bump" near 90°.

incident from a certain direction (θ_i, ϕ_i). Its units are inverse steradians (sr^{-1}). Because it accounts for directionality as well as in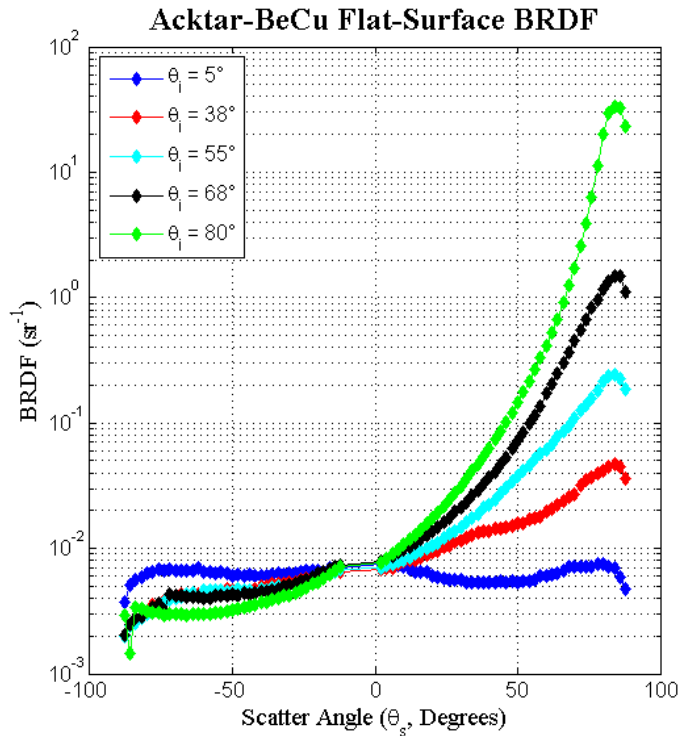cident power, BRDF is extremely informative in terms of characterizing the scattering properties of various materials, and is needed as an input to our stray light model in order to characterize the scatter properties of a surface.

In Section 5.2 we show the results of modeling flight scale starshades with edges made out of each candidate material. The BRDFs and TIS (Table 4-2) of each material were measured by TSW and served as inputs to those particular model runs. An example BRDF measurement, taken for the flat and coated region of the Acktar-BeCu sample, is shown in Figure 4-3 for characterization. All other flat-surface BRDF data is included in the data package submitted with this report. The measurements were taken in-plane, meaning that ϕ_i and ϕ_s were always

0°/180°. Sweeps over scatter angle (from -88° to 88°) were taken at five different incidence angles (5°, 38°, 55°, 68°, and 80°). Due to the symmetry of the coatings, out-of-plane BRDF measurements did not yield new optical performance data, so were not measured.

Incident Angle (°)	TIS (%) @ 633 nm				TIS (%) @ 488 nm			
	Acktar Ti	Acktar BeCu	Enbio Ti	Enbio Al	Acktar Ti	Acktar BeCu	Enbio Ti	Enbio Al
0	1.49	2.11	5.25	5.49	1.08	1.38	3.29	3.75
15	1.64	2.31	5.51	5.69	1.10	1.44	3.36	3.89
30	1.90	2.66	5.84	5.97	1.23	1.64	3.68	4.22
45	2.40	3.36	6.73	6.71	1.57	2.10	4.53	4.99
60	3.46	4.87	9.12	8.58	2.26	3.03	6.61	6.59
75	5.34	8.03	13.70	11.82	3.39	4.74	10.27	8.79
89.5	5.48	8.29	13.65	11.76	3.48	4.90	9.98	8.60

Table 4-2: TIS values for each sharp edge sample, measured by TSW. The TIS at 488 nm is consistently lower than that at 633 nm. In general, TIS @488 ~0.65 * TIS @ 633 nm.

4.3 SHARP EDGE MEASUREMENTS

The majority of time spent by TSW was on measuring the scatter properties of the sample edges. Characterizing scatter from edges in a lab setting is not a typical measurement, and thus has no prescribed procedure. Below, we document the experimental approach in detail and explain our choices regarding the approach that we chose in order to make these measurements.

20

4.3.1 MEASUREMENT SYSTEM

The flight starshade-edge-telescope system will operate in a wide variety of orientations. In particular, the angle of the incoming sunlight varies between 45° and 85° (from starshade normal, see Figure 2-1), the angle between the optical axis of the telescope and starshade normal can vary between 0° and 15° (Figure 2-1), and the orientation of the starshade edge varies over all angles based on starshade rotation, petal orientation (with respect to the sun), and the location of each differential edge segment along the petal curve. In order to span this range of possible flight orientations in our experiment, we defined an experimental geometry (shown in Figure 4-4) with three variable parameters: incident angle (θ_i), polar/scatter angle (θ_p, θ_s), and azimuth angle (θ_{az}).

The incident angle is the angle that the incoming laser light makes with sample normal, and is analogous to the angle of the incoming sunlight with respect to starshade normal. The polar angle is the angle between sample normal and the optical axis of the detector, and is analogous to the angle of the optical axis of the telescope with respect to starshade normal. The azimuth angle is the angle that allows sample rotation about its normal, and is analogous to the varying orientation of the starshade edge with respect to the incoming sunlight (orthogonal rotation to the incident angle). The azimuth angle is defined as 0° when the edge is vertical and 90° when the edge is horizontal. Scatter angle, θ_s, is defined as the angle between the detector and the specular beam. It serves the same purpose as the polar angle but is measured from the specular beam rather than sample normal. Thus θ_s varies depending on the incident angle of the beam. All the above angles are measured with the sample edge as the origin.
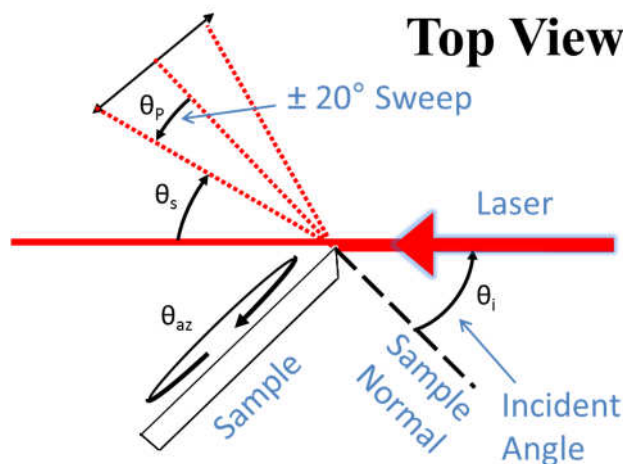

Figure 4-4: Top view of the experimental geometry. With the laser directly aligned on the sample edge, CASI takes sweeps in polar angle, θ_P (or scatter angle, θ_s), for various combinations of incident angle (θ_i) and sample azimuth (θ_{az}). Here the sample is oriented at θ_i=45° and a sample azimuth of 0°. The bevel of the sharp edge sample faces the light source, which in a flight system would minimize the amount of illuminated edge visible to the telescope.

In order to allow for the necessary degrees of freedom in the experiment for the relevant orientations to be measured, a custom sample holder was fabricated (Figure 4-5). The holder is a Newport mount with part of its outer ring removed to allow laser light to come in from large angles (defined as θ_i). The designed rotation of the Newport mount allows the sample to be rotated about its normal (defined as θ_{az} above, see left panel of Figure 4-5).

After review of trial data taken by TSW on an uncoated sample, we decided to take measurements at the orientations listed in Table 4-3. For each of the four sharp edge samples, scans across the selected polar angles (-20° to 20° about sample normal) were taken for each combination of incident and azimuth angle. This resulted in a large data set for each sample that effectively spans all orientations relevant to the on-orbit system. For the θ_{az}=0° (vertical edge and incident plane measurements corresponding to diffraction) case, data was taken from polar angles of -84° to 84° (rather than -20° to 20°) in 2° steps.

The entire range of orientations was repeated using blue (488 nm) and red (633 nm) lasers as the incident beam, resulting in a total of 384 edge scans. Both lasers were circularly polarized to eliminate any interaction that the straight edge may have with a linearly polarized source.
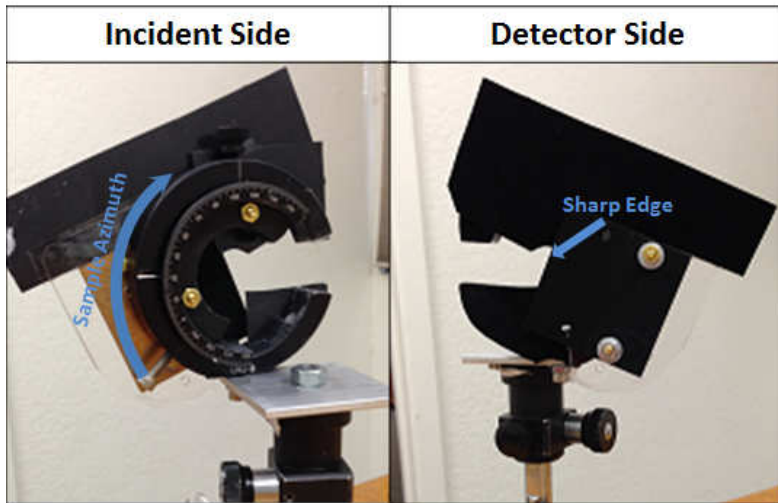

Figure 4-5: The custom sample holder imaged from the incident side (left) and the detector side (right). The holder is a Newport mount modified to allow an off-axis beam to hit the sample edge unhindered. Care was taken to block all stray light except that scattering from the sharp edge. The mount rotates (see left) to vary the sample azimuth angle from 0° (vertical edge) to 90° (horizontal edge).

Parameter	Values (Degrees)	Rationale
θ_i	-30, -40, 45, 55, 65, 75, 80, 85	The effective incidence angles cover -85° to -45° and 45° to 85°. Negative values represent edge illuminated on the far side of the starshade (opposite the sun). The geometry of the sample holder limited testing at negative angles.
θ_P	-20 to 20, 2 degree steps	Range more than spans relevant flight orientations (0-15°).
θ_{az}	0, 20, 40, 60, 80, 90	With symmetry, spans relevant flight orientations. This was the most difficult angle to set in the experiment.

Table 4-3: Scatter measurement test parameters collected for most of the samples with ranges that covered the geometry shown in figure 2-1.

4.3.2 ALIGNMENT

Figure 4-6 shows the operational experimental setup. As is pointed out in the figure, approximately half of the beam is reflected off the face of the test sample back in the incident direction, while approximately half of the beam is transmitted past the sample. Only a very small fraction of the beam is scattered from the sample edge itself, and the amount of light incident on the edge varies depending on the beam alignment. Much care was taken to align the setup so that exactly half of the beam was transmitted past the sample (T = 0.5) for each measurement, but

Figure 4-6: The TSW setup with the laser and test sample in place. Half of the beam reflects back from the sample and half is transmitted past the sample. Only a small amount of the beam scatters from the edge.

transmission values still varied between T= 0.4 and T = 0.6 over the entire data set, likely due to small misalignments present in the setup that were magnified during the collection of the angle sweeps.
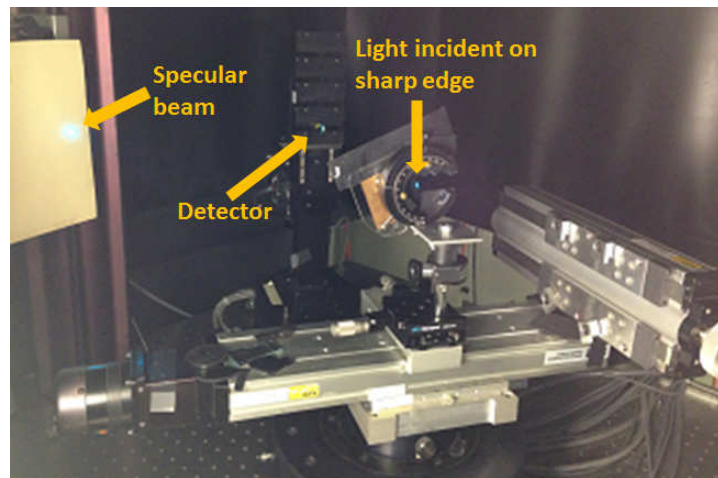
22

Given the obvious effect that these alignment variations have on the data, TSW performed an analysis to quantify how the changing alignment of the beam on the edge influences the measurements. For sample azimuths of 0° and 90°, data was taken at various configurations of beam alignment on the sample edge and compared to the nominal T = 0.5 case (Figure 4-7). From this data, the following relationship between alignment and measurement was found:

$$Alignment\ Correction = 1 - 3.5(T - 0.5)^2$$ **Equation [1]**

Equation [1] represents the blue trend line in Figure 4-7. Note that for high azimuth angles, the correction does not fit the data well for values of Transmission >0.6. Since all measurements had T between 0.4 and 0.6 this is expected to be a very small contributor to the measurement error.

For each measurement sweep the transmission of the beam past the sample was measured and the alignment correction equation was used to scale the data and cancel out the effects of any misalignment. For the majority of the data set the alignment-corrected data differed from the uncorrected data by an average of 0.4%.
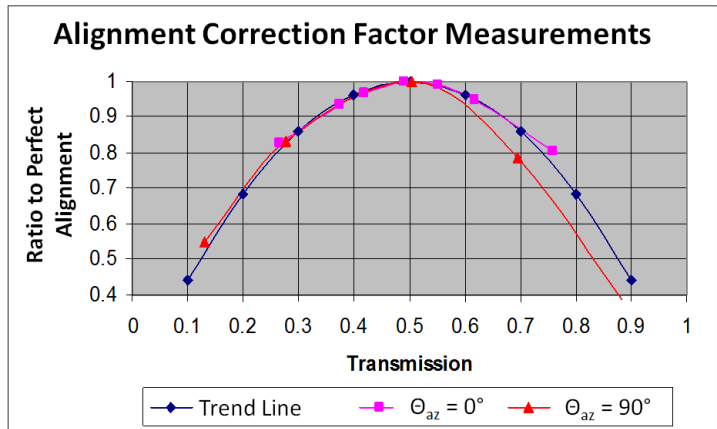
Figure 4-7: Measurements taken to calibrate how measurements change with the varying alignment of the laser on the edge. This relationship was used to cancel the effects of alignment on our measurements.

4.3.3 MEASUREMENTS

Figures 4-8, 4-9, and 4-10 are representative of the different ways we cut through the data in post processing. These plots are meant to characterize the data set, and are made from just a fraction of the data taken by TSW. The complete data set, along with the post-processing results, is included in the data package submitted with this report.

It should be noted that, while the CASI scatterometer reports measurements in BRDF units (sr^{-1}), the data can't be interpreted in the conventional sense. This is because only a fraction of the sample beam is incident on the edge, so normalization by the beam power (inherent in the calculation of BRDF) results in a scale-factor difference from what the normalization usually achieves. The direction of sample normal (from which the BRDF angles are measured) is also unclear for a sharp edge. In spite of these caveats, the scatter measurements performed by CASI on the sample edges are still indicative of their functional/relative performance, and can be processed to yield quantitative results (see Section 5.3).

23

4.3.3.1 Constant θ$_i$ (Incident Angle)

Figure 4-8 shows the measurements taken from the sharp edge of each sample for a constant θ$_i$ of 75° for various values of θ$_{az}$ (angles are defined in Section 4.3.1). This incidence angle was chosen to be included in this report because it represents a flight orientation where the sun is nearly edge-on to the starshade, an orientation that is favored in many mission architectures. Each separate plot is for a different sample, and each plot shows sweeps of data for various azimuth angles. As can be seen, scatter from the sample edges generally decreases as azimuth angle increases. This trend holds up for each sample across the entire range of θ$_i$ except for the negative values (θ$_i$ = -30°, -40°), where the trend is reversed. From this trend we can speculate that, for the flight system, differential edge segments oriented horizontally with respect to the incoming sunlight will scatter less light than those oriented vertically for petal edges on the sun-facing side of the starshade.

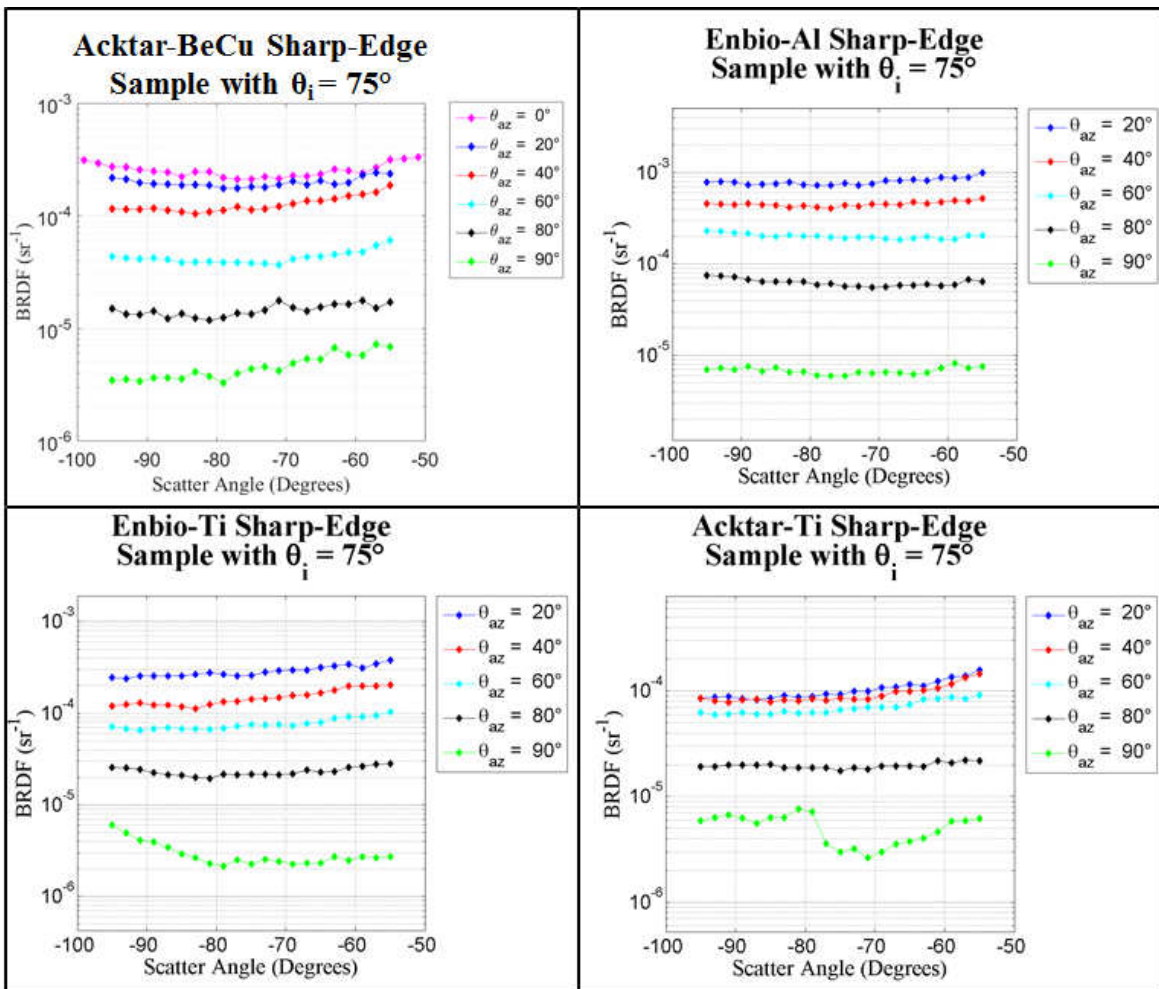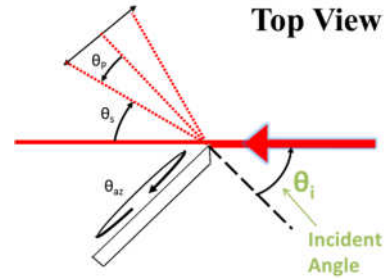**Figure 4-8:** Test sample BRDF edge scatter measurements at various θ$_{az}$ with θ$_i$ = 75°. Plots are shown for each sample: Acktar-BeCu (top left), Enbio-Al (top right), Enbio-Ti (bottom left), and Acktar-Ti (bottom right). On the x-axis is scatter angle, θ$_s$, which represents the angles that the detector swept over (see Figure 4-4). In general, edge scatter decreases as θ$_{az}$ increases.

24

4.3.3.2 Constant θ$_{az}$ (Azimuth Angle)

Figure 4-9 shows the measurements taken from the sharp edge of each sample for a constant θ$_{az}$ of 20° for various incidence angles. This azimuth angle was chosen to be included in this report somewhat arbitrarily since all of the values for θ$_{az}$ apply equally to the range of flight orientations. Clearly apparent from the plots is that scatter from negative θ$_{i}$'s is far less bright than scatter from positive θ$_{i}$'s. This is true across the entire data set and indicates that, on-orbit, the petal edges on the sun-facing side of the starshade should scatter more light towards the telescope than the petal edges on the side of the starshade opposite to the sun. This result was expected and helps to justify our experimental setup. In general the edge scatter tends to decrease as θ$_{i}$ decreases, but the trend is not as strong as the others discussed. The multiple exceptions to this trend (including the Acktar-BeCu plot shown in Figure 4-9) throughout the data set indicate that the dependence of scatter strength on the angle of the incoming sunlight is somewhat non-trivial.
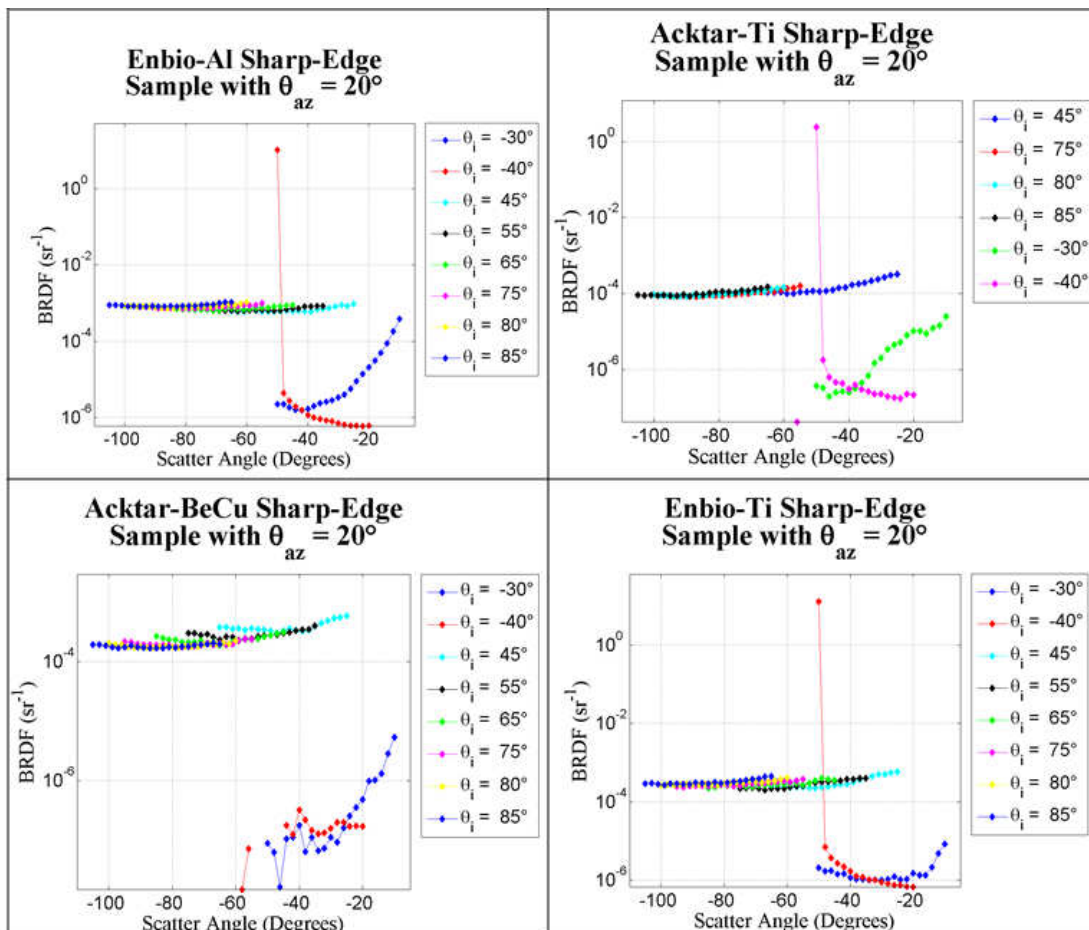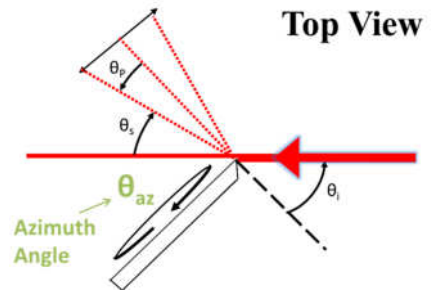
Figure 4-9: Test sample BRDF edge scatter measurements at various θ$_{i}$ with θ$_{az}$ = 20°. Plots are shown for each sample: Enbio-Al (top left), Acktar-Ti (top right), Acktar-BeCu (bottom left), and Enbio-Ti (bottom right). On the x-axis is scatter angle, θ$_{s}$, which represents the angles that the detector swept over (see Figure 4-4). In general, edge scatter decreases as θ$_{i}$ decreases. The high value in the θ$_{i}$ = -40° scan is an artifact from the sample holder and limits the feasible scan for this incidence angle.

4.3.3.3 Sample Comparisons

Figure 4-10 plots the measurements taken from the sharp edge of each sample for a constant θ_{az} = 20° and θ_i = 75°. At the specific orientation shown, Acktar-Ti is the top performer, followed by Acktar-BeCu, Enbio-Ti, and Enbio-Al.

Since the scatter performance of the on-orbit starshade edge is represented by a superposition of all of the orientations measured in the lab, a candidate edge structure that performs best at a single orientation (like the Acktar-Ti sample in Figure 4-10) is not guaranteed to be the best candidate for flight. Instead, performance across the entire range of orientations tested in the lab must be considered.

Figure 4-10: Test sample BRDF edge scatter measurements with θ_i=75° and θ_{az} = 20°. Different color lines refer to different samples. On the x-axis is scatter angle, θ_s, which represents the angles that the detector swept over (see Figure 4-4). At this orientation the Acktar-Ti sample performs best.

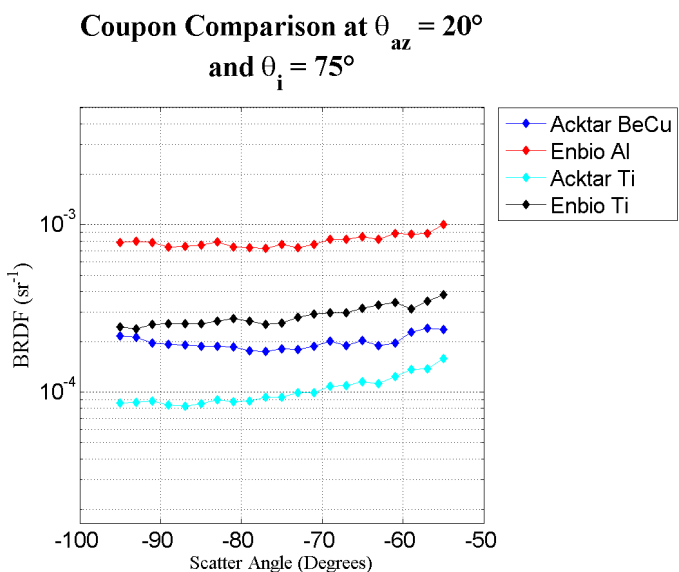To quantify the overall scatter performance of the different sample edges, we developed a numerical performance rating procedure that was applied to the entire data set measured for each sample by TSW. First, the degrees of freedom in the data were reduced by taking the trimmed mean (mean disregarding outliers) of the CASI sweeps across θ_s. Thus, for any combination of θ_i and θ_{az} each sample had one corresponding measurement value (rather than 20). For each sample the averaged measurement values were then summed up and scaled, yielding a numeric value that takes into account the scatter performance of the sample edge at every orientation tested. Table 4-4 shows the numeric performance ratings for each sample and Figure 4-11 shows the ratios of the performance ratings to the top performer. Since a lower performance rating corresponds to better scatter performance, we found that across all orientations the Acktar-Ti edge performs best, performing 1.6x better than Acktar-BeCu, 1.9x better than Enbio-Ti, and 4.8x better than Enbio-Al. Numeric performance ratings were also calculated by taking the single central value of θ_s for each combination of θ_i and θ_{az} (rather than taking the trimmed mean). These ratings are also reported in Table 4-4 and Figure 4-11. The results are very similar to those that use the trimmed mean.

	Scatter Angles Averaged	Single Scatter Angle
Ti Acktar	19	17
BeCu Acktar	30	26
Ti Enbio	36	32
Al Enbio	91	87

Table 4-4: Numeric ratings of the scatter performance of each sample edge. A lower rating corresponds to higher performance.
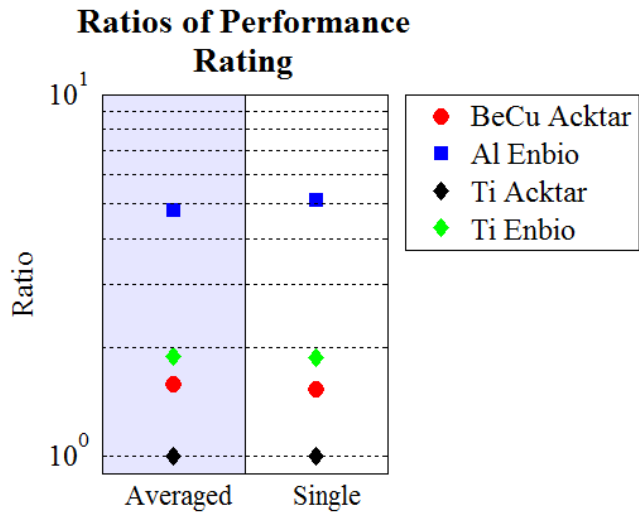

Figure 4-11: Ratios of the performance rating of each sample edge to the top performer: Acktar-Ti.

4.3.4 UNCERTAINTIES

Above, one uncertainty already observed was the correction factor for the Transmission correction factor (Figure 4-7) for large azimuth angles and larger than 0.5 T. To investigate other potential error sources of the test setup, several repeatability experiments were run. The repeatability of the edge scatter measurements was investigated by taking multiple CASI scans of the Acktar-BeCu sample edge for various experimental orientations. Though this repeatability data is not plotted in this report, it is included in the accompanying data package.

The repeatability investigation revealed that if the sample is not taken out and placed back into the sample holder, CASI scans repeat almost exactly. If the sample is removed and replaced, however, the measured BRDF data changes. Since each removal/replacement of the sample leads to a different segment of the sample edge being illuminated by the incident beam, this result suggests that the issues with repeatability have to do with edge uniformity.

To investigate the uniformity of the sample edges we oriented each sample with the edge horizontal (θ_{az} = 90°), oriented the laser to have normal incidence (θ_i = 0°), and oriented the detector at θ_p = -45°. These parameters remained fixed while each sample was moved horizontally in its own plane in steps roughly equal to a third of the illuminated spot diameter. The results of this investigation are shown in Figure 4-12. If the edge were perfectly uniform, the scatter signal would remain constant. The aluminum sample clearly has higher variability than the other samples, particularly at the extremes of the scan. For all samples, the scatter signal varies significantly across the scan. The cause of this variability is believed to be edge non-uniformity either due to manufacturing variability in machining or coating, or simply handling damage. Given that the samples were shipped multiple times and handled extensively for measurements, the presence of handling damage on the sample edges is plausible. Due to this inherent uncertainty regarding our measurements, the experimental numbers moving forward should be considered to be uncertain by a factor of 2.
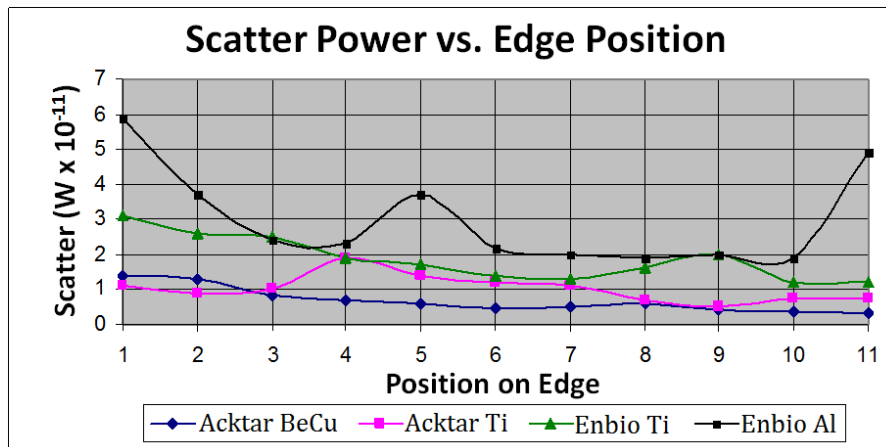
Figure 4-12: The measured scatter signal vs. the position of the laser beam on the edge is plotted for each sample. The scatter signals from each sample vary by factors of about 2.5 depending on the segment of edge illuminated.

4.4 POST-ENVIRONMENTAL OPTICAL PERFORMANCE

While the environmental testing documented in Section 3.3 yields important information regarding the physical durability of our candidate materials in mission environments, just as important in order to guarantee starshade edge performance throughout the mission lifetime is that the scattering properties of the coating don't degrade. As a preliminary test of the resilience of the optical properties of our candidate materials to a space environment, the optical performance of the coated flats of the test coupons that underwent thermal cycling and humidity exposure was measured by TSW; these results were then compared with those of the pristine samples. Samples that underwent cyclic abrasion and tape adhesion testing were not tested by TSW.

Measurements at all lab orientations were not needed to compare the scattering properties of the pristine samples to the environmentally exposed samples. Measurements of the environmentally exposed samples were taken at one orientation: $\theta_i = 80°$, from $\theta_p = -88°$ to $+88°$ (in 2° steps). Comparisons of pre- and post-environmental scatter performance for each sample are shown in Figure 4-13. As can be seen, only small differences between the pristine coatings and the environmentally exposed coatings were measured, and these are likely due to the uncertainties regarding edge uniformity characterized in Section 4.3.4 above. These preliminary results are encouraging as they indicate that the scatter properties of our candidate materials likely won't degrade during the mission lifetime, though a more rigorous testing effort in the future is required.
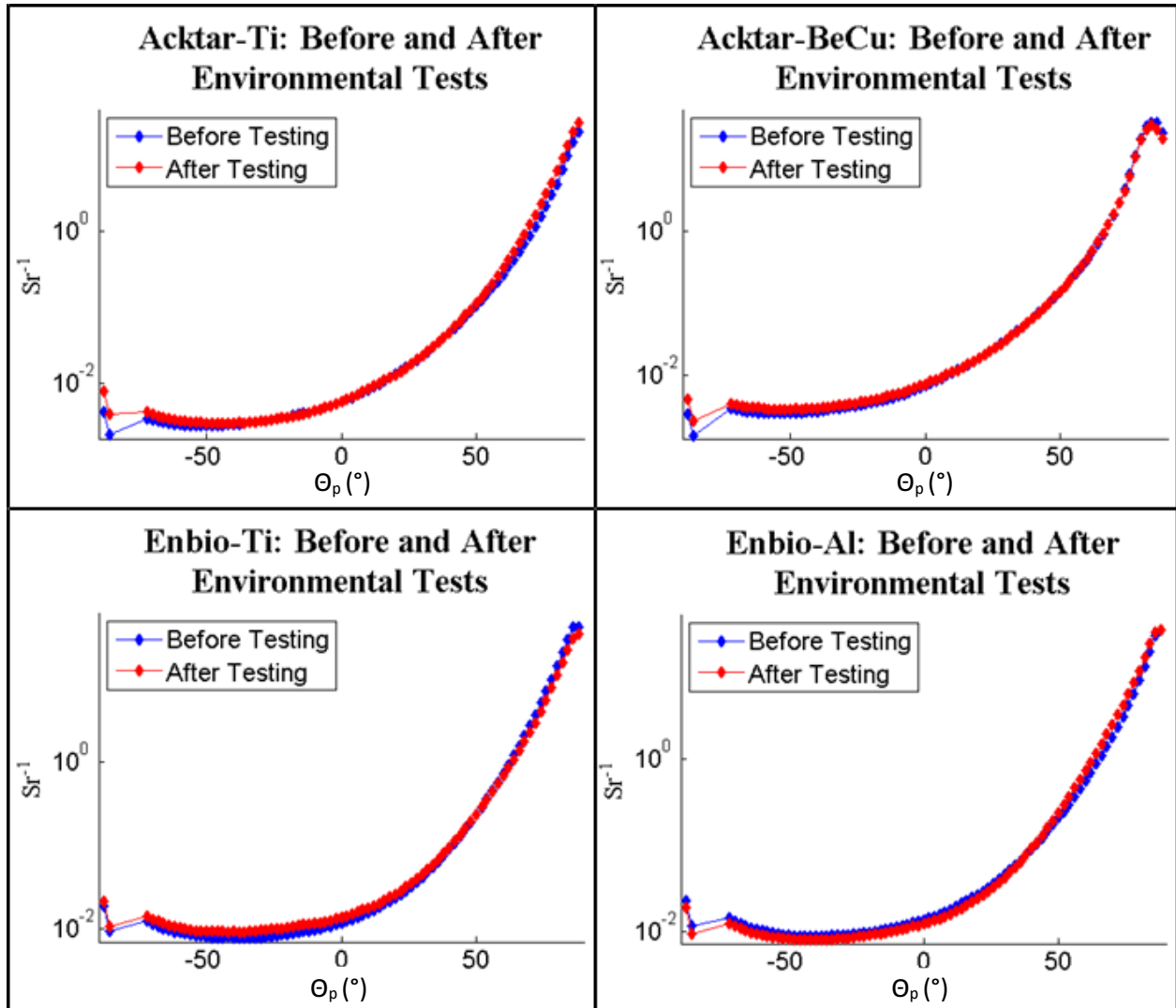
Figure 4-13: Scatter properties of each coated sample flat before (blue) and after (red) thermal cycling and humidity exposure. Measurements were taken at $\theta_i = 80°$. No significant differences in performance were measured.

5 STRAY LIGHT MODEL

The previous stray light simulation developed by NG in TracePro required many scaling factors to bridge the large dynamic range of the model[8]. Additionally, the NG model showed disagreement by a factor of approximately 10^4 with a physics-based model developed by JPL[7,16]. In order to advance our stray light modeling capabilities and also to shed light on the discrepancies between the previous models, we teamed with Photon Engineering (PE), recognized as experts in stray light modeling, to use their expertise to model the stray light scattering from the starshade edge, independent of previous work done by either NG or JPL. Further review of this discrepancy suggested that many other differences in the architecture as modeled could in fact account for most of the difference, such as starshade size (edge length), separation, and edge scatter properties. However, the different architectures have not as yet been analyzed by the same modeling code to validate that hypothesis. Future work has been identified to resolve this but it was not a central part of our study, merely an impetus to develop a more

complete model. Development of this model by PE complies with the stray light simulation aspect of our TDEM milestone. In Table 5-1 we break down the simulations run and their relevance to the milestone.

Simulation	Purpose	Milestone Relevance
Model results using candidate edge properties	Performance predictions for flight scale starshades with edge properties analogous to those of the sharp edge coupons developed/measured in sections 3 and 4	Characterizes on-orbit performance of constructible edges. Helps to calibrate a relationship between blackness, edge RoC, and on-orbit scatter performance
Simplified model of the TSW lab setup	Simulate the sharp edge measurement system created by TSW and compare the simulation results to lab measurements	Correlates the model with physical measurements, establishing its validity

Table 5-1: The simulations (presented below) run by PE, their purpose within our TDEM effort, and their relevance to our TDEM milestone.

5.1 INITIAL MODEL DESIGN AND INPUTS

The model at PE was developed in FRED, a commercial stray light software package capable of simulating the propagation of light through any optomechanical system by raytracing. Specific details about the FRED software are not provided in this report, but are available on the software website linked in the references. The extensive use of FRED for various stray light modeling applications adds to the credibility of our model, though we recognize that ray trace models do have inherent challenges with high attenuation scenarios such as this one. Significant work went into the modeling effort to address this challenge for the starshade system model by using many techniques developed at PE.

Because a key feature of the JPL model was the inclusion of a diffracted light component, we considered adding this to our model during the development of the white paper. However, due to the nature of the FRED software (it uses purely raytracing) and schedule constraints, we did not add it in. Future additions to the model could be considered. The comparison of the model to the measured data, particularly as shown in Figure 4.8, provides an upper limit on the contributions of diffraction to the stray light performance of the sharp edge samples which is in contrast to the JPL results[16]. This is further discussed in Section 5.3.

A CAD model of the NWO starshade (shown in Figure 5-1) is used as the input to the simulation to allow precise representation of the Hypergaussian petal shape and edge radius of curvature, rather than just an edge approximation using ellipsoids as in the original TracePro-based model. For all of our simulation analyses under this TDEM we assume the New Worlds Observer architecture, as documented by the ASMCS[4]. We recognize that there are many variations of a starshade mission which have been or are currently under study. However, to provide the best value under this study, we will use our NWO mission design since it is readily available and we believe scalable to other architectures based on, for example, separation, total edge length, and edge RoC.
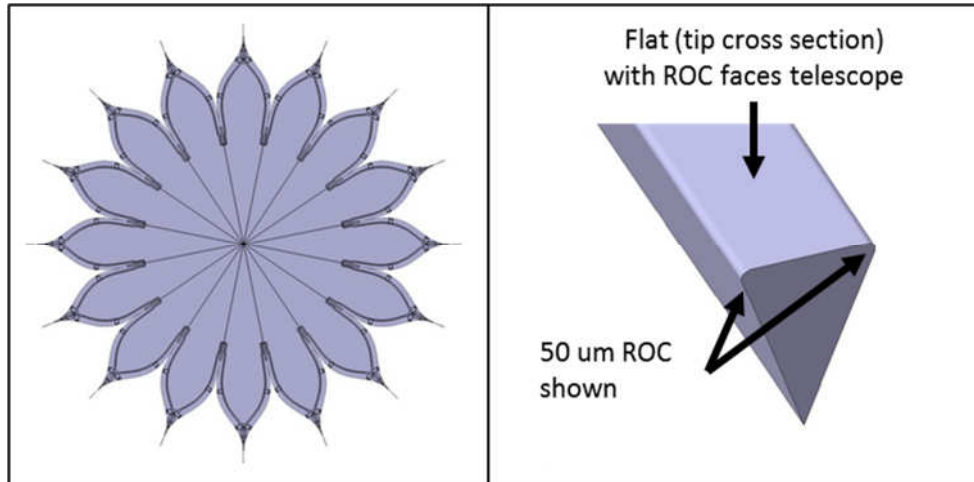
Figure 5-1: The starshade CAD model used in the FRED model. At left is the full starshade and at right is a close up view of a tip. A 50 μm edge RoC on both telescope-facing edges of the tip is shown in the figure.

The FRED model geometry of a single starshade petal is depicted in Figure 5-2. The geometry is a direct import of the NG-supplied CAD models, with hinges and face structures removed. The starshade face is assumed to be a perfect absorber, while the edge is assigned the scatter properties of the edge material under consideration. For the results presented in Section 5.2, six different edge architectures are simulated: a black Graphite edge with a 10 μm RoC, a black Graphite edge with a 50 μm RoC (the general NWO edge design), an Acktar-coated Titanium edge (20 μm RoC), an Acktar-coated BeCu edge (20 μm RoC), an Enbio-coated Titanium edge (20 μm RoC), and an Enbio-coated Aluminum edge (20 μm RoC). BRDF data is what characterizes the scatter properties of the edge in the simulation. For the Graphite edge this data was provided to PE by NG, collected on a previous NG effort and shown in Figure 5-3. The Acktar- and Enbio-coated edges are made of the various substrate/coating combinations tested in Section 4; the BRDF data that characterizes the edge performance was provided to PE by TSW (see Section 4.2) for these four cases.
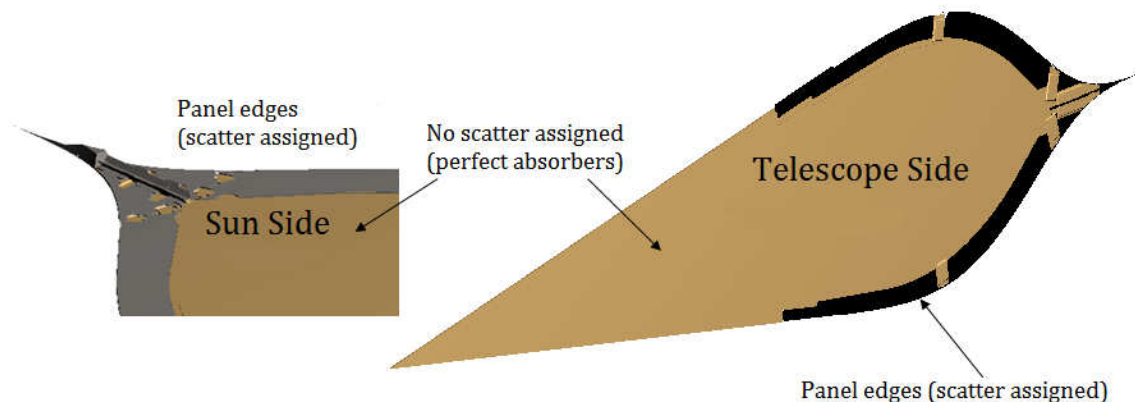

Figure 5-2: Starshade petal design as modeled by PE from the CAD drawing. Petal edges are assigned scatter properties via BRDF measurements of the edge material under consideration (grey). The face of the petals/starshade is modeled as a perfect absorber (gold). The tip deployment elements are also included in the CAD model (structure on backside).

31
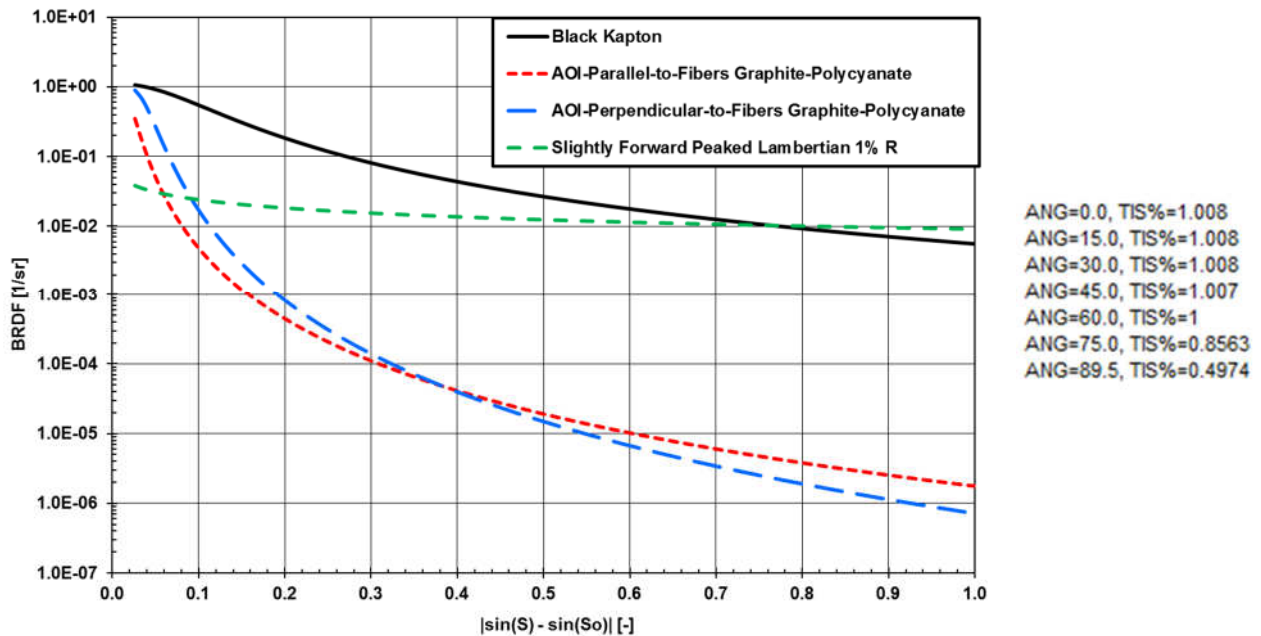
Figure 5-3: Log-log plot of previous BRDF measurements used for initial PE modeling and performance comparison. Data from previous NG program measured at 575 nm. S= Scatter Angle (θ_s), So=Specular (incident) angle. TIS, as a function of incident angle, is given on the right.

Launching rays from the location of the sun is computationally inefficient due to its large distance from the starshade and would lead to extremely long computation times. Instead of dealing with these long processing times, emitting surfaces equivalent to those that would be created by the incident sunlight were constructed along each petal edge. These emitting surfaces are a construction of planar triangular facets that provide a starting location for the rays (Figure 5-4). Each petal edge is sampled at 7500 points along its length and fit with a corresponding emitter that is oversized relative to the edge RoC to ensure full illumination of the edge from all directions. The use of triangular facets for the emitter geometry allows for an easy calculation of the surface area, which is used to scale the source flux. The starting ray positions are randomly distributed over the emitter surface. Every point launches rays randomly into a cone whose angular width matches that of the sun; the axis of the emission cone is aligned to the direction vector of the sun. The emitters are monochromatic, and their strength is calculated by integrating the solar spectrum to get the solar incident irradiance.

Figure 5-4: The complex emitter geometry for a given petal edge minimized run time by optimizing the incident rays. Along each edge, oversized triangular facets trace the edge profile and shoot rays, informed by the orientation/irradiance of the sun, toward the starshade edge for analysis.

32

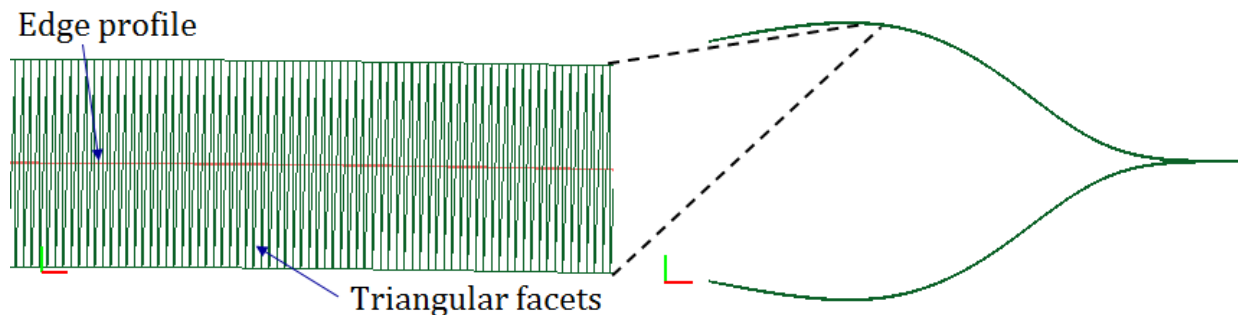Following the NWO architecture, the simulation uses a 60 m tip-to-tip starshade with an 80,000 km separation from the telescope (Figure 5-5). The telescope has a 4 m primary with a 10% obscuration and is modeled as a perfect geometric lens with an EFL = 73.666 meters. Rays reaching the telescope are focused onto an ideal detector with 5 µm pixels and a total size of 80 µm x 80 µm. Neither starshade rotation nor the Point Spread Function (PSF) of the telescope are accounted for in the model, but are addressed analytically as described in Section 5.2.2.

Two orientation angles were varied in the models: the starshade orientation (azimuth angle) and the direction of the incoming sunlight (incident angle). These angles are shown in Figure 5-6. The definitions of *azimuth* and *incidence* here are consistent with those defined for the sharp edge samples in Section 4.3.1, and are both measured from starshade normal. In the model, the optical axis of the telescope remains parallel to starshade normal rather than being varied as its analog was for the measurements made by TSW (θ_p from Section 4.3.1). For the Graphite edge cases

Figure 5-5: The scale of the simulated on-orbit starshade system.

simulated, models were run at 9 incidence angles (45° – 85° at 5° increments) and 4 azimuth angles (0°, 5.625°, 11.25°, and 16.875°). The range of azimuth angles was selected to span the range between sunlight directly illuminating the starshade tips and directly illuminating the starshade valleys. After the initial simulations it was found that the results did not vary significantly with azimuth angle, so we narrowed our azimuth range to 0° and 11.25°. The range of incidence angles spans the relevant orientations of the flight system.

Figure 5-6: Visualizations of the orientation angles varied in the simulation. These angle definitions reflect those defined for the sharp edge sample section (θ_i and θ_{az}, see Section 4.3.1), but for the full starshade geometry.

Table 5-2 lists all the required inputs of the model, their values, and how they were supplied.

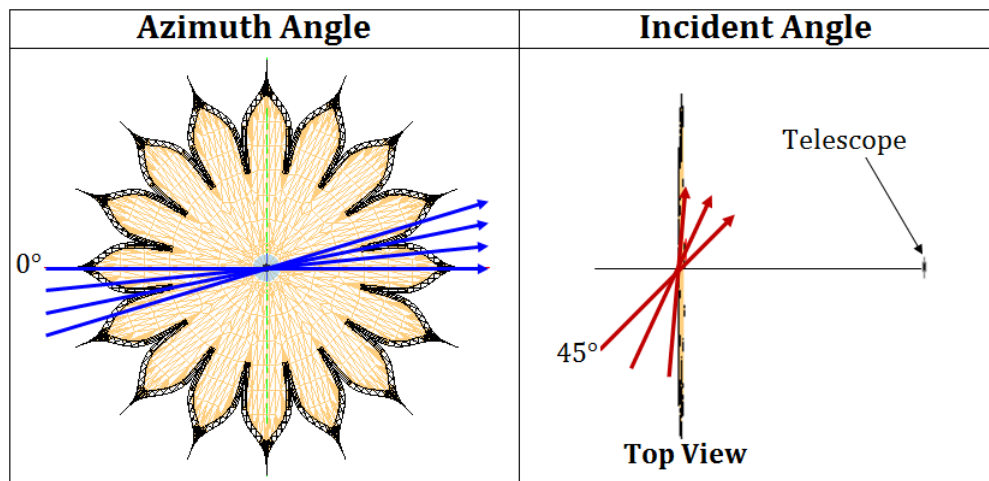|	Input	Notes

Light Source	• ASTM E-490 Solar Spectrum
	• Numerically integrated to inform monochromatic emitters
	  ❖ Full spectrum E_0 = 1368 W/m^2
	  ❖ 0.4 – 0.9 μm E_0 = 760 W/m^2
		• Emitting surface constructed along each petal edge rather than propagating rays from the sun to the starshade

Starshade Shape	• CAD models supplied by NG. NWO design: 60 m tip-to-tip, Hypergaussian edge profile	• Hinges and face structures removed • Starshade face modeled as perfect absorber
Starshade Edge	• BRDFs @ 633 nm of edge material characterize edge scatter properties • Provided by NG for Graphite • Provided by TSW for candidate materials (Acktar/Enbio-coated edges)	• Edge RoC 10 and 50 μm for Graphite • Edge RoC 20 μm for candidate materials (roughly matches RoC on test samples)
Telescope	• Perfect geometric lens, 4 m aperture • 1.264 m secondary (10% obscuration) • Effective Focal Length: 73.666 m	• 80,000 km separation from starshade (NWO architecture)
Orientation	• Incident angles: 45° – 85°, 5° steps • Azimuth angles: 0°, 5.625°, 11.25°, 16.875° (Graphite); 0°, 11.25° (Other)	• 0° = tip towards sun • 11.25° = valley towards sun

Table 5-2: A summary of all the inputs to the PE stray light simulation of the starshade edge.

5.2 MODEL RESULTS

Here we present the results of the simulations of the flight system run by PE along with an analysis of their impact on the design requirements for the starshade edge. The model parameters replicate the general NWO architecture as described in Section 5.1, assuming six different edge cases. The black Graphite edge cases were run as an initial check on the simulation and also as a baseline case to be compared to the results of the previous NG simulated edges. The Enbio- and Acktar- coated edges were run in order to characterize the flight performance/requirements of the edge concepts that have been optically tested (Section 4) and proven to be manufacturable (Section 3) under other parts of this TDEM.

The BRDF used in the model is strictly for the 633 nm case. We have insufficient data to apply a spectral BRDF against the solar spectrum as shown in **Figure 7**. However, the BRDF measurements at 488 nm as shown in Table 4-2 are ~65-70% that of the BRDF at 633 nm while the total power is <25% more. Given the solar spectrum and the relatively flat BRDF of our coatings[14], we believe that using the 633 nm value is a reasonable approach to scale to the integrated solar energy. We scale to Watts collected using the input total solar power in the 400 – 900 nm band based on the fraction of scatter at 633 nm to calculate the power shown in the model results below.

Standard Solar Spectrum

http://rredc.nrel.gov/solar/spectra/am0/
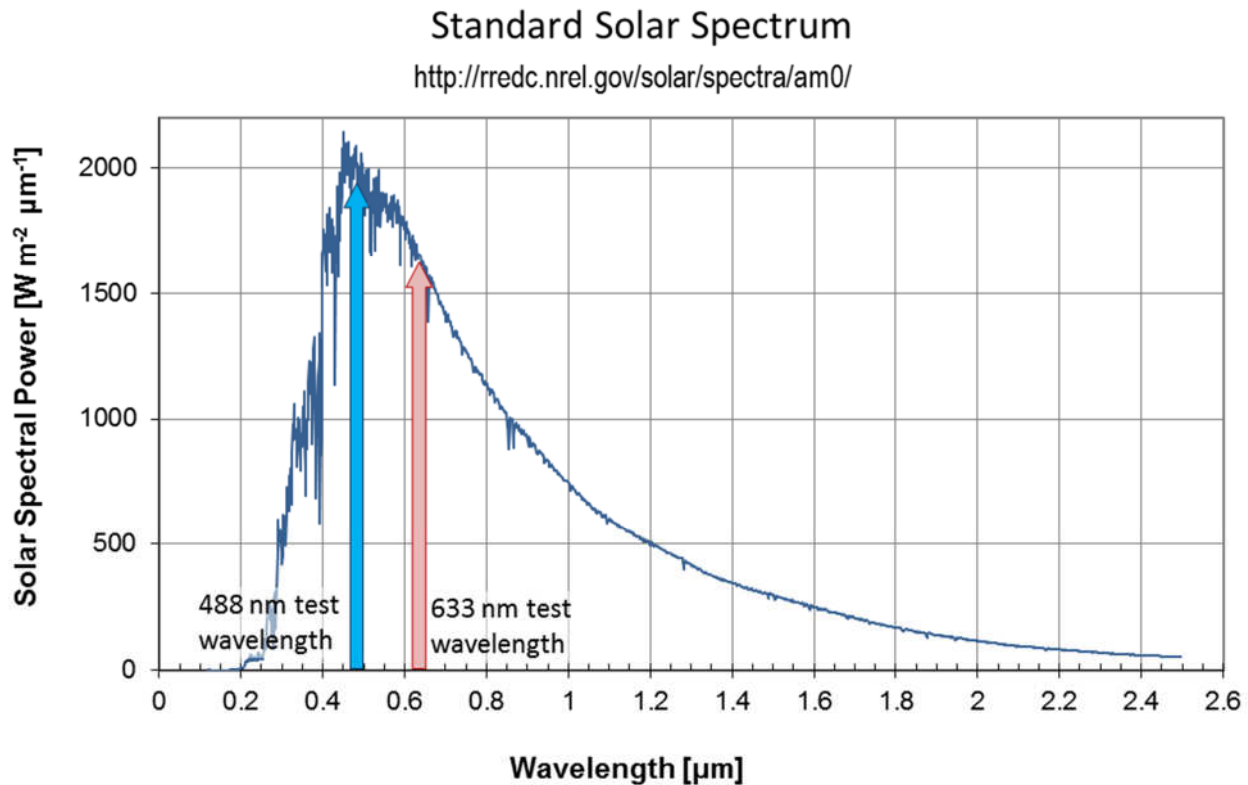
Figure 7: Solar spectrum and relative BRDF measurements show that using 633 nm data is relatively conservative for the 0.4 – 0.9 micron wavelength region.

The solar illumination was rastered over the specified incident and azimuth angles, with E_0 (760 W/m^2) scaled by the cosine of the incident angle for each run. The model outputs geometric detector irradiance at 2 resolution levels. For the low resolution case each pixel is 5 µm across and subtends an angle of 0.067 µrad (the telescope PSF is Nyquist sampled). This approach gives results at a flight-like resolution. We also ran high resolution cases for each orientation/edge case where each pixel is 0.3125 µm across (16x the resolution of the flight-like case). This allowed us to identify which parts of the starshade contribute most to the overall scatter background. These model details remain the same for all results included in this report (namely the results presented in this subsection and in the data package submitted separately).

We present model results for each material type in Section 5.2.1. Detector irradiance plots are shown from the high resolution runs and the low resolution runs. The plots and numbers supplied by PE do not take into account the blurring effects of the telescope PSF, nor do they consider the blurring due to the possible rotation of the starshade throughout integration. Once the data was given to NG we convolved the flight resolution detector irradiance arrays with a normalized mask representative of the telescope PSF. To approximate the starshade rotation we applied a linear motion filter separately to each quadrant of the images. The rotational motion was simulated in a very simple way by aligning the linear motion filter tangential to the radius in each quadrant which blurs out the flux in translation, and then the 4 images were stacked. These blurring techniques are illustrated in Figure 5-8. For the motion filter, we simulated starshade rotation over 22.5°, the angular width of one petal. While this is a very simple simulation of starshade motion, it shows the potential benefits of rotating the starshade during an observation.
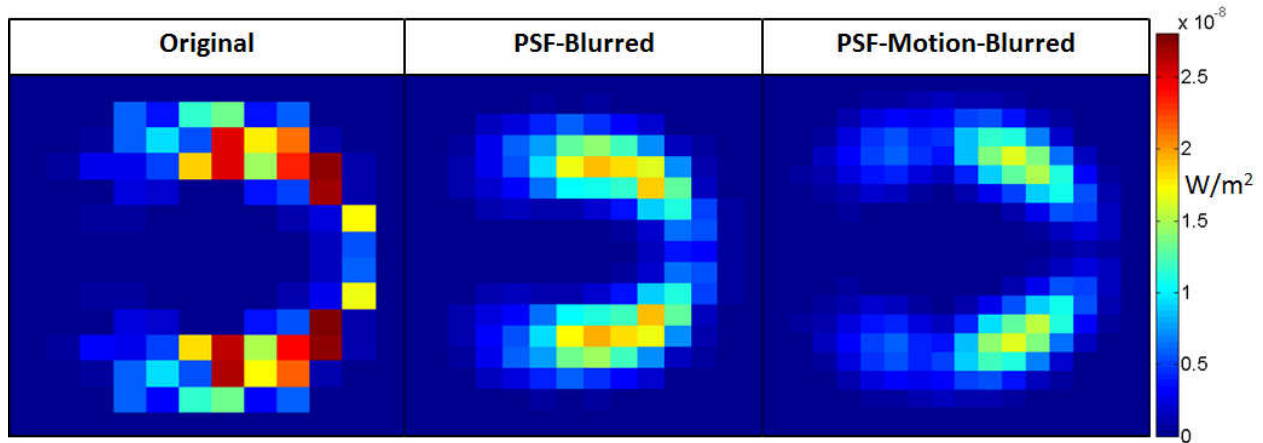
Figure 5-8: Example of the originally supplied detector irradiance image (left), the PSF-blurred image (center) and the PSF-motion-blurred image (right). The total integrated flux over the detector remains constant, but the peak irradiance is lower in the blurred images.

5.2.1 RESULTS: EXAMPLE PLOTS/NUMBERS

Here we present a subset of the data set provided to us by PE. Complete data sets for both resolution cases are included in the data package submitted with this report. The case for which we present the data in Figures 5-9 through 13 and associated tables, θ_i = 75° and θ_{az} = 0°, was chosen because it is an orientation likely to be heavily used on-orbit. An analysis relating our results to the actual flight system follows in Section 5.2.2.

Graphite (10 and 50 μm RoC)

Figure 5-9: Irradiance images in the detector plane for the NWO starshade modeled with Graphite edges with $\theta_i = 75°$ and $\theta_{az} = 0°$. Images are shown in both high and low resolution for each edge RoC. Blurring effects due to the telescope PSF/starshade rotation are not accounted for.

Azimuthal Angle (°)	Incident Angle (°)	RoC (μm)	Integrated Flux (W)	Ratio (50/10)	Peak IR (W/m²)	Ratio (50/10)	Peak IR (PSF-Blur)	Peak IR (PSF/Motion)
0	75	10	1.55×10^{-18}	10.26	1.33×10^{-8}	5.71	4.63×10^{-9}	2.98×10^{-9}
		50	1.59×10^{-17}		7.59×10^{-8}		3.41×10^{-8}	2.59×10^{-8}
5.625	75	10	2.36×10^{-18}	5.34	2.30×10^{-8}	4.74	5.99×10^{-9}	4.05×10^{-9}
		50	1.26×10^{-17}		1.09×10^{-7}		3.18×10^{-8}	1.95×10^{-8}
11.25	75	10	2.85×10^{-18}	5.86	2.01×10^{-8}	5.72	9.06×10^{-9}	5.87×10^{-9}
		50	1.67×10^{-17}		1.15×10^{-7}		5.47×10^{-8}	3.59×10^{-8}
16.875	75	10	2.06×10^{-18}	6.12	1.97×10^{-8}	5.08	6.33×10^{-9}	3.78×10^{-9}
		50	1.26×10^{-17}		1.00×10^{-7}		3.58×10^{-8}	2.39×10^{-8}

Table 5-3: Integrated flux and peak irradiance values for the 10 and 50 μm RoC Graphite starshade models. The ratios of the 50 μm case to the 10 μm case for both integrated flux and peak irradiance are approximately 5, indicating edge performance that scales linearly with edge RoC. Peak irradiance values are reported for the original image, the PSF-blurred image, and the PSF-motion-blurred image.
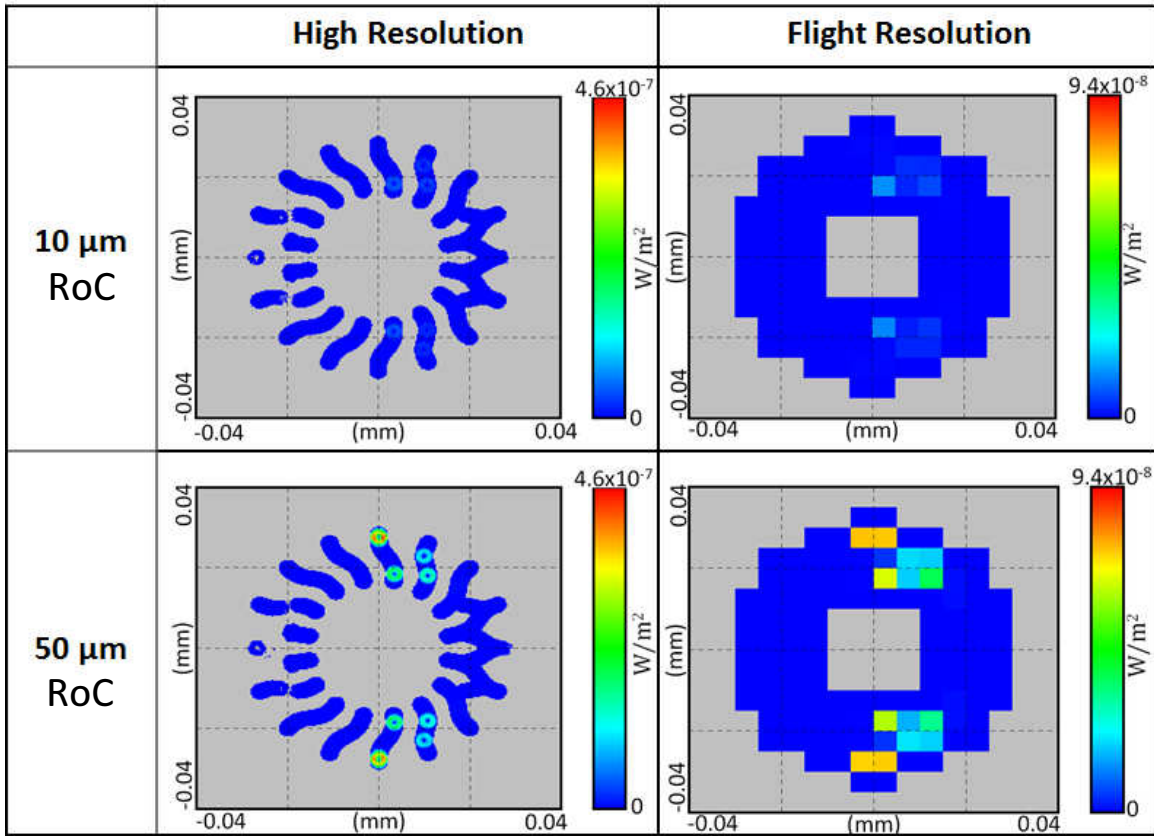
Acktar-Coated Titanium

Figure 5-10: Irradiance images in the detector plane for the NWO starshade modeled with Acktar-coated Titanium edges with $\theta_i = 75°$ and $\theta_{az} = 0°$. Images are shown in both high and low resolution. Blurring effects due to the telescope PSF are not accounted for. The edge RoC is 20 μm.

Azimuthal Angle (°)	Incident Angle (°)	RoC (μm)	Integrated Flux (W)	Peak IR (W/m²)	Peak IR (PSF-Blurred)	Peak IR (PSF/Motion)
0	75	20	1.64×10^{-17}	2.78×10^{-8}	1.93×10^{-8}	1.67×10^{-8}
11.25	75	20	1.65×10^{-17}	3.85×10^{-8}	2.17×10^{-8}	1.78×10^{-8}
0	55	20	1.78×10^{-17}	4.60×10^{-8}	2.46×10^{-8}	2.01×10^{-8}
11.25	55	20	1.74×10^{-17}	4.12×10^{-8}	2.68×10^{-8}	2.01×10^{-8}

Table 5-4: Integrated flux and peak irradiance values for the 20 μm RoC Acktar-coated Titanium starshade models. Peak irradiance values are reported for the original image, the PSF-blurred image, and the PSF-motion-blurred image.

38

© 2016 Northrop Grumman Corporation

Acktar-Coated BeCu

Figure 5-11: Irradiance images in the detector plane for the NWO starshade modeled with Acktar-coated BeCu edges with $\theta_i = 75°$ and $\theta_{az} = 0°$. Images are shown in both high and low resolution. Blurring effects due to the telescope PSF are not accounted for. The edge RoC is 20 μm.

Azimuthal Angle (°)	Incident Angle (°)	RoC (μm)	Integrated Flux (W)	Peak IR (W/m^2)	Peak IR (PSF-Blurred)	Peak IR (PSF/Motion)
0	75	20	2.37×10^{-17}	4.02×10^{-8}	2.79×10^{-8}	2.42×10^{-8}
11.25	75	20	2.37×10^{-17}	5.51×10^{-8}	3.23×10^{-8}	2.63×10^{-8}
0	55	20	2.59×10^{-17}	7.24×10^{-8}	3.69×10^{-8}	2.94×10^{-8}
11.25	55	20	2.52×10^{-17}	6.17×10^{-8}	3.93×10^{-8}	2.93×10^{-8}

Table 5-5: Integrated flux and peak irradiance values for the 20 μm RoC Acktar-coated BeCu starshade models. Peak irradiance values are reported for the original image, the PSF-blurred image, and the PSF-motion-blurred image.
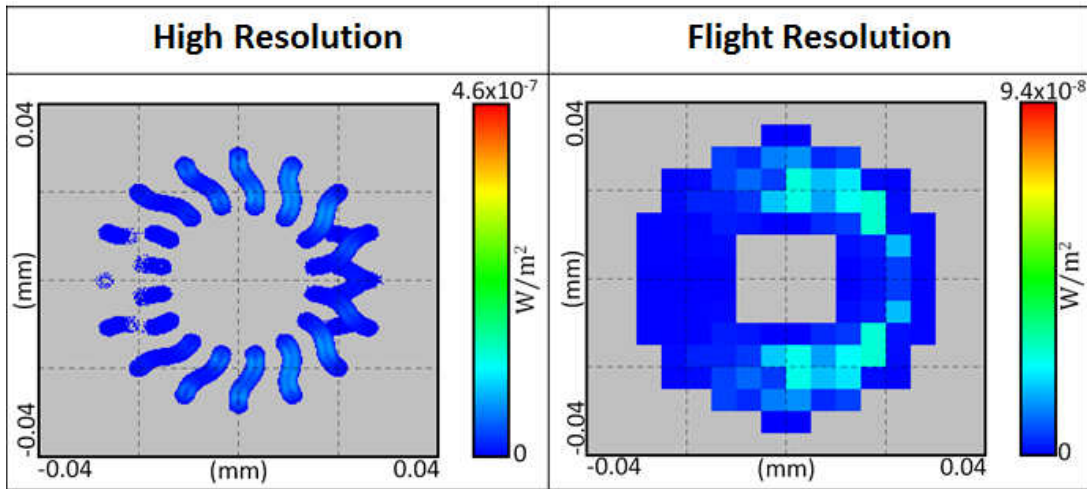
Enbio-Coated Titanium

Figure 5-12: Irradiance images in the detector plane for the NWO starshade modeled with Enbio-coated Titanium edges with $\theta_i = 75°$ and $\theta_{az} = 0°$. Images are shown in both high and low resolution. Blurring effects due to the telescope PSF are not accounted for. The edge RoC is 20 µm.

Azimuthal Angle (°)	Incident Angle (°)	RoC (µm)	Integrated Flux (W)	Peak IR (W/m²)	Peak IR (PSF-Blurred)	Peak IR (PSF/Motion)
0	75	20	4.07×10^{-17}	8.19×10^{-8}	5.18×10^{-8}	4.46×10^{-8}
11.25	75	20	4.09×10^{-17}	9.46×10^{-8}	6.05×10^{-8}	4.79×10^{-8}
0	55	20	4.47×10^{-17}	1.38×10^{-7}	6.57×10^{-8}	5.16×10^{-8}
11.25	55	20	4.40×10^{-17}	1.23×10^{-7}	7.10×10^{-8}	5.38×10^{-8}

Table 5-6: Integrated flux and peak irradiance values for the 20 µm RoC Enbio-coated Titanium starshade models. Peak irradiance values are reported for the original image, the PSF-blurred image, and the PSF-motion-blurred image.
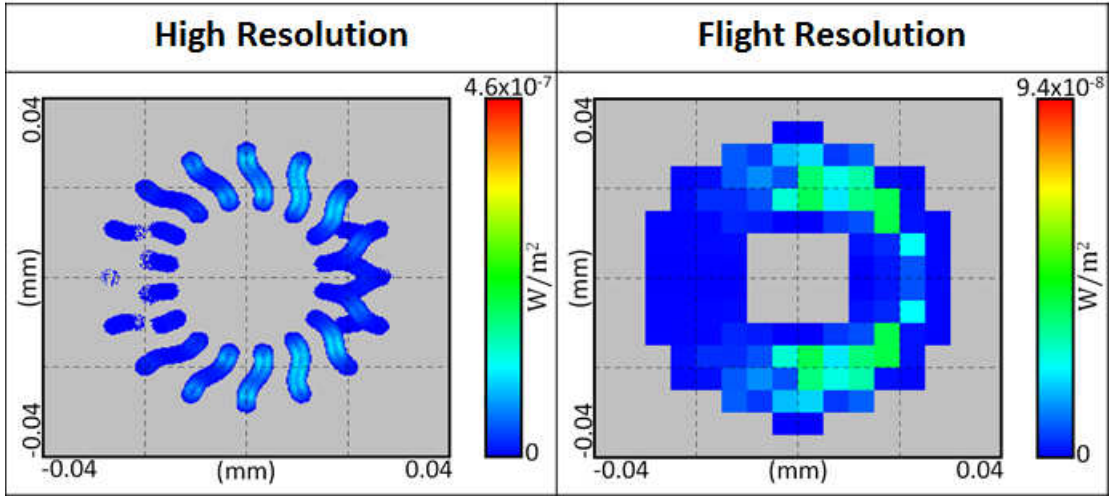
Enbio-Coated Aluminum
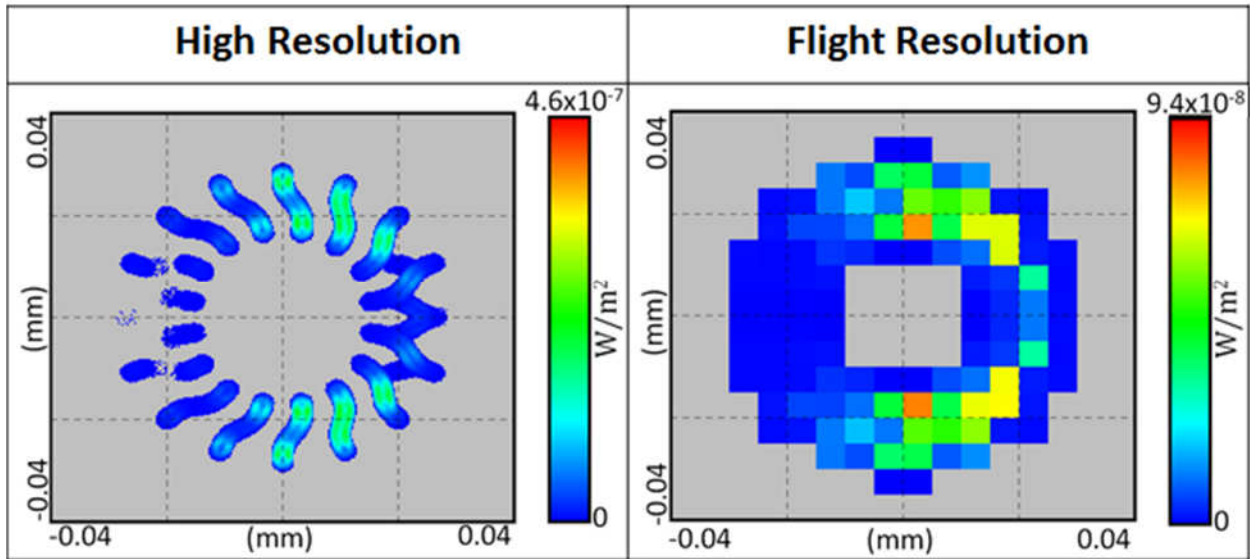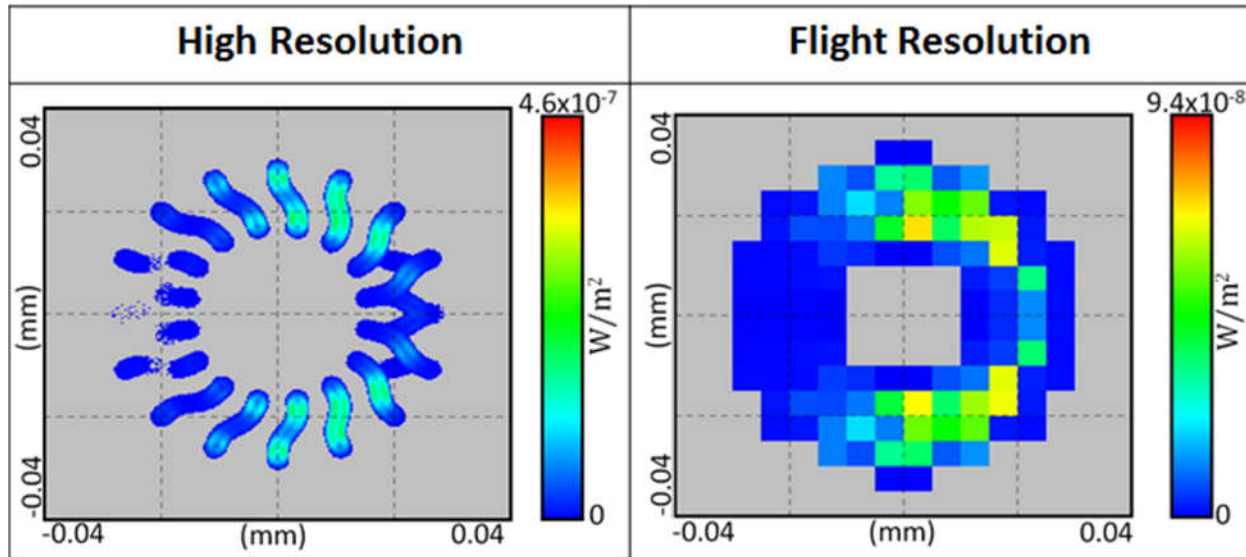

Figure 5-13: Irradiance images in the detector plane for the NWO starshade modeled with Enbio-coated Aluminum edges with $\theta_i = 75°$ and $\theta_{az} = 0°$. Images are shown in both high and low resolution. Blurring effects due to the telescope PSF are not accounted for. The edge RoC is 20 µm.

Azimuthal Angle (°)	Incident Angle (°)	RoC (µm)	Integrated Flux (W)	Peak IR (W/m²)	Peak IR (PSF-Blurred)	Peak IR (PSF/Motion)
0	75	20	4.00×10^{-17}	7.31×10^{-8}	4.93×10^{-8}	4.23×10^{-8}
11.25	75	20	4.01×10^{-17}	9.00×10^{-8}	5.74×10^{-8}	4.59×10^{-8}
0	55	20	3.93×10^{-17}	1.14×10^{-7}	5.62×10^{-8}	4.44×10^{-8}
11.25	55	20	3.89×10^{-17}	1.01×10^{-7}	6.08×10^{-8}	4.66×10^{-8}

Table 5-7: Integrated flux and peak irradiance values for the 20 µm RoC Enbio-coated Aluminum starshade models. Peak irradiance values are reported for the original image, the PSF-blurred image, and the PSF-motion-blurred image.

5.2.2 RESULTS: ANALYSIS

As can be seen in the results presented above for the Graphite cases, the edge with a RoC of 50 µm is about 5x brighter in both peak irradiance and integrated flux than the 10 µm RoC case. This 5x factor is consistent throughout the entire range of orientations tested by PE (see the separate data package) and indicates that the optical performance of the starshade edge scales linearly with its RoC. With this knowledge, we scaled the Graphite results to a 20 µm edge RoC so that its performance could be directly compared to the other cases run.

Figure 5-14 shows the direct comparisons of the integrated flux (left) and peak irradiance (right) for each edge configuration (Graphite results are scaled to a 20 µm RoC to match the other edge cases). In general, the measured data for all models is functionally similar. According to the model Graphite is the top performer, followed by Acktar-coated Titanium, Acktar-coated BeCu, Enbio-coated Aluminum, and Enbio-coated Titanium, respectively. Due to the diffuse nature of the coatings, the Acktar- and Enbio-coated edges show higher flux levels (by 5x to 10x) than the Graphite edges. However, based on our experience building scale models of starshades with graphite polycyanate material, it is unknown if the edges could be fabricated to shape with very sharp edges. Cut edges of graphite fibers in the composite show degradation, becoming "furry" which is not consistent with the edge shape requirements as it is a material. It is worth noting is that the simulated performance of each measured edge (Acktar and Enbio) is directly correlated with the measured TIS for each sample given in Table 4-2 (lowest TIS shows the lowest flux levels, etc…). This is in agreement with the performance predictions made by TSW (Section 4.3.3.3), except that the Enbio Ti edge and the Enbio Al edge have switched positions.
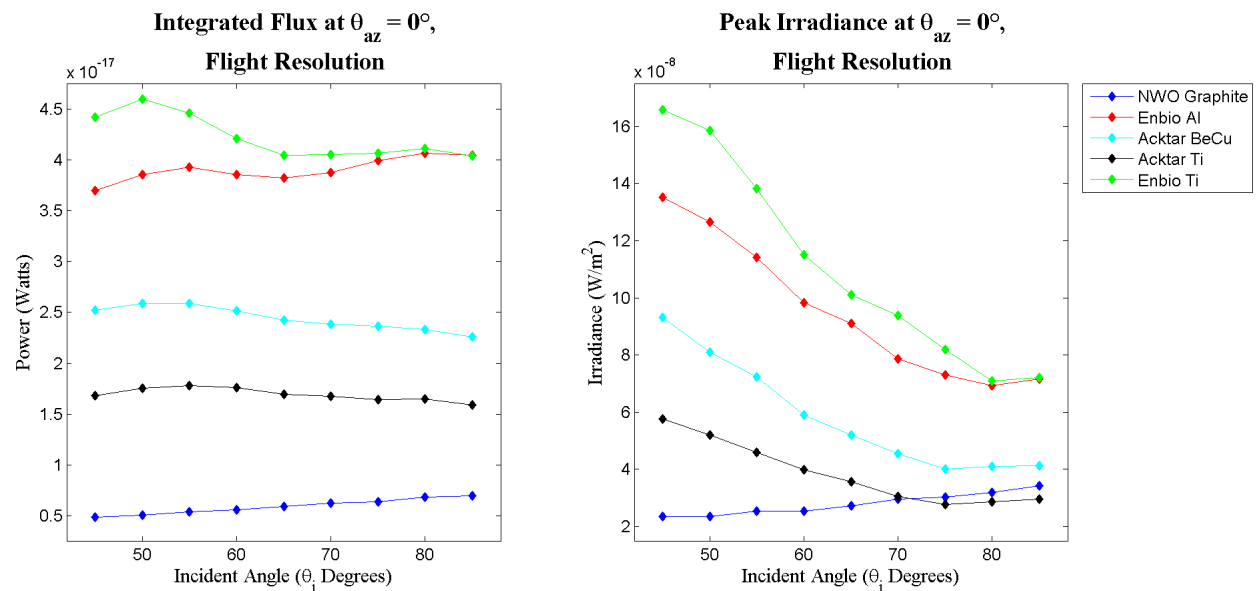
Figure 5-12: The integrated flux (left) and peak irradiance (right) output by the model for each edge coating at flight-like resolution, with θ$_{az}$ = 0°. Results at different azimuths were very similar to those plotted. The Graphite model (RoC 50 µm) was linearly scaled to a 20 µm RoC for comparison purposes.

We found that lower incidence angles have higher flux contributions. Similarly, edges oriented more vertically with respect to the incoming sunlight (θ$_{az}$ around 0°, as defined in Section 4) seem to contribute more than those oriented horizontally. As was expected, the model results also confirm that petal edges on the side of the starshade opposite the incoming sunlight scatter significantly less light into the telescope than those on the sun-facing side.

To translate our data into performance estimates for a starshade mission we compared the pixel brightnesses in the simulation data (scaled to the V band and PSF/motion blurred) to the V band pixel brightnesses resulting from a 31st and 33rd magnitude planet. In order to localize our analysis to various sections of the starshade edge, we split the starshade up into four regions as shown in Figure 5-15, taking into account the symmetry of the system about the incoming sunlight. Considering the starshade in parts rather than as a whole allows us to better understand the effect that the scatter from the starshade edge has on the overall sensitivity to planets of the system. For the top two performers (Acktar Titanium and Graphite), the results of this analysis are shown graphically in Figure 5-16.
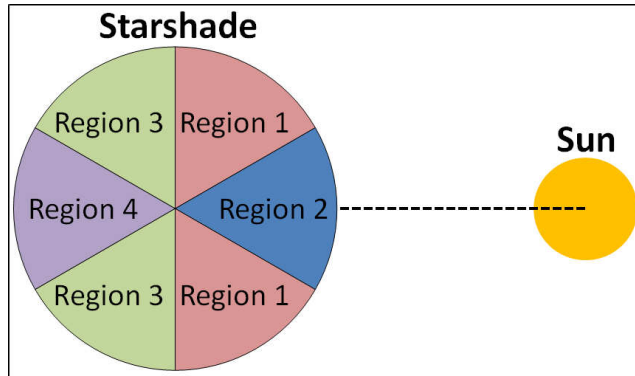
Figure 5-15: The regions of the starshade from which we calculated individual edge brightnesses. Regions take the symmetry of the system into account.
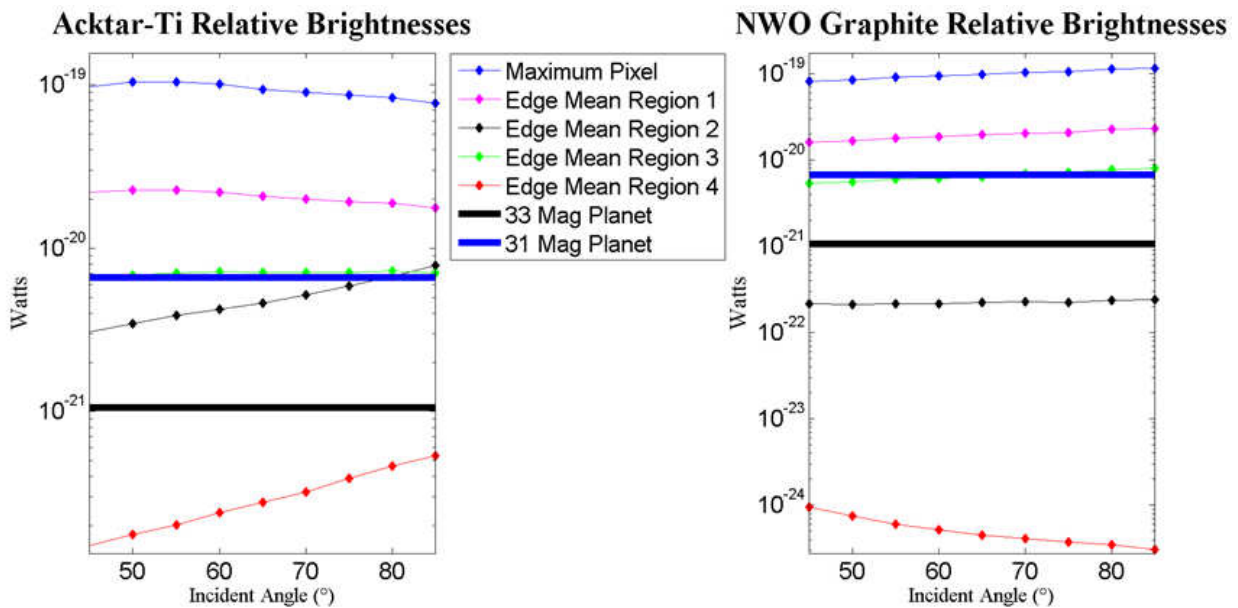
Figure 5-16: Model predictions of the pixel brightnesses along the edge of various regions of a flight scale NWO starshade. The graph at left is for a Titanium starshade edge coated with Acktar Magic Black ™, and the graph at right is for the Graphite starshade edge concept. Both have a RoC of 20 μm.

For each 20 μm edge design the brightest pixel is about an order of magnitude brighter than a pixel within the PSF of a 31st mag planet and two orders brighter than that of a 33rd mag planet. Region 1 is consistently predicted as the brightest region of the starshade edge, ranging from approximately 2x to 10x the 31st mag planet level, depending on the edge case considered. Region 4 is consistently predicted as the dimmest region of the starshade edge, with brightnesses well below the 33rd mag planet level for both an Acktar Titanium edge and a Graphite edge.

43

Table 5-8 shows a derived edge RoC requirement for each edge configuration, assuming that the scatter performance of the starshade edge scales linearly with RoC (supported by the data shown in Figure 5-9 and Table 5-3). Currently there is no real benchmark for the required stray light

Edge Design	Below 31 Mag Level (% of Edge)	Below 33 Mag Level (% of Edge)	Derived RoC (μm)
Enbio Al	17%	~17%	7
Enbio Ti	17%	~17%	8
Acktar BeCu	~25%	17%	12
Acktar Ti	~35%	17%	18
Graphite	~48%	33%	17

Table 5-8: The amount of the starshade edge (in percent) below the different planet levels. Also reported is the RoC required for each edge concept to have average brightnesses in Regions 2, 3, and 4 below the 31st mag level.

performance of the starshade edge. In order to detect a 33rd mag planet, for example, it may be that the starshade edge closest to the planet must be no brighter than the planet signal, or it may be that the edge could be much brighter than the planet signal and the planet would still be detectable.

The RoC requirements presented in Table 5-8 are based on the criterion that the three dimmest regions of the starshade edge (Regions 2, 3, and 4) must be below the signal level of a 31st magnitude planet over all incidence angles. This criterion corresponds to 67% of the starshade circumference being below the 31st mag level, and was selected by the NG team as an anchor point from which our results could be translated to engineering requirements. Additional analysis has been started to take the flux distribution maps as convolved with the telescope PSF and add to it a notional planet signal, stellar leakage signal, exozodi, and detector noise characteristics. This analysis should lead to an "effective" IWA for the configuration modeled as a function of the planet brightness and region it happens to land in. These data can be used to evaluate completeness models and the observational efficiency for a starshade, with some additional uncertainty due to the model uncertainties.

5.3 MODEL VALIDATION

In an effort to establish the validity of the simulation, a study was carried out by PE to correlate their ray trace analysis with the measurements made by TSW. This resulted in the construction of a simplified version of the starshade model that simulates the TSW lab setup. The outputs of the simplified model were then compared directly to the TSW measurements. Details and results regarding this validation effort are documented below.

5.3.1 TEST CONFIGURATION MODEL DETAILS

To compare the FRED scatter model to the TSW scatter measurements, PE created a simple FRED model that duplicates the test configuration and measurement process implemented by TSW. The sharp edge sample in the simulation has an edge modeled as a perfect cylinder with a 20 μm RoC with no surface roughness, an idealized model compared to the measured samples. As in the full starshade model, scatter properties are assigned to the sample edge via the BRDF data provided by TSW (Section 4.2).

A diagram of the setup of the simulation is shown in Figure 5-17. As can be seen, the setup directly mimics the TSW experimental setup diagramed in Figure 4-4. The laser is modeled as an incoherent Gaussian beam that illuminates the sample edge over 15 mm and generates scattered rays that propagate to an ideal detector subtending 0.00178 steradians (solid angle matches the angle subtended

by the experimental detector). This is likely one source of modeling error as the laser beam, while put through the polarizers to generate equal S and P polarization, is still a coherent source. The beam is also not purely Gaussian, though the measurements taken to calculate the Transmission correction factor (Figure 4-7) show that it's relatively close.

Though the CASI scatterometer at TSW outputs edge scatter data in units of BRDF (sr^{-1}), the data can't be interpreted in a conventional sense because the sample beam is large relative to the RoC of the test samples. Considering the dependencies of BRDF on incident power and also on sample normal, this is problematic because as noted in Section 4.3:

1. There is no true 'sample normal' for an edge
2. The full beam is not incident on the edge, and there is no ability (by the test instrument) to resolve the area of the illuminated edge

Top View

Figure 5-17: Diagram of the FRED simulation of the experimental setup. The system directly mimics the measurement system of the TSW lab.

Using the conversion factor developed in Section 4.3.2 to account for the small alignment shifts during a data collection, and then comparing the way FRED calculates power to the measurement technique, a relationship between the model and the measurement was derived with the left hand side representing the model and the right hand side representing the measurement.

$$\frac{P_{model}}{\Omega} = \frac{P_{laser} \cdot BRDF_{TSW} \cdot \cos\theta_s}{1 - 3.5 \cdot (T - 0.5)^2}$$

Equation [2]

P_{model} is the power in the detector plane output by the PE model; Ω is the solid angle subtended by the detector in the lab setup and is equal to 0.001781 steradians; P_{laser} = 2.56 x 10^{-3} Watts is the power of the laser (both 633 nm and 488 nm are modeled); θ_s is the angle between the detector and sample normal (as seen in Figures 4-4 and 5-17); as before, T is the transmission fraction of the laser (~0.5, Section 4.3.2). This equation transforms the CASI BRDF measurement into a measurement of power per unit solid angle as calculated by the model by multiplying out the dependence on incident power and scaling by the cosine of the scatter angle. This approach is documented in Stover (2015) [15] and more information is available in The ScatterWorks final report (submitted with this report).

5.3.2   VALIDATION RESULTS

The PE simulation of the TSW lab setup was run at all relevant orientations (see Table 4-3), varying the sample azimuth angle, the incident angle of the laser (θ_i), and the angle between the detector and sample normal (θ_s). For each orientation of sample azimuth and θ_i, a sweep of measurements over θ_s was simulated. Using Equation [2] the correlation between the model and the measurements could be generated by calculating the ratio between the two sides of Equation [2] ("Ratio") and the Variance in the ratio for each sweep (21 values) at a given azimuth and incidence angle. The results for the Acktar-Titanium sample with a 633 nm laser are listed in Table 5-9. The results are also plotted in Figure 5-18 for both the Ratio and the Variance for all sample azimuth and incidence angles. The data are clearly better correlated with smaller variances at high incidence angle (closer to edge on) and low azimuth
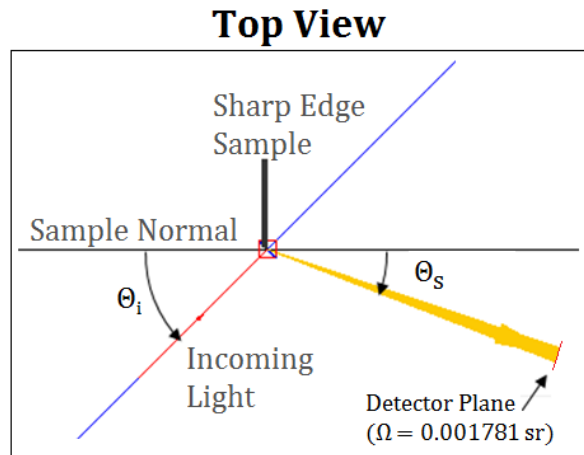
45

angle. The complete correlation analysis, performed for all four test coupons at both wavelengths (633 nm and 488 nm), is included within the data package submitted with this report.

Sample Azimuth (°)	θ_i (°)	Ratio (Meas/Model)	Variance	Sample Azimuth (°)	θ_i (°)	Ratio (Meas/Model)	Variance
20	45	9.23	36.77	60	75	14.39	1.72
20	55	4.05	1.76	60	80	11.39	0.69
20	65	3.06	0.36	60	85	9.12	0.51
20	75	3.35	0.07	80	45	231.76	3377.91
20	80	3.46	0.09	80	55	128.36	468.29
20	85	3.88	0.07	80	65	76.79	106.74
40	45	28.46	210.11	80	75	42.79	14.72
40	55	20.55	59.41	80	80	28.43	4.44
40	65	12.45	6.87	80	85	17.67	1.18
40	75	7.25	0.78	90	45	5.05×10^5	4.99×10^{10}
40	80	6.18	0.31	90	55	5.3×10^5	3.07×10^{10}
40	85	5.55	0.13	90	65	1.16×10^6	2.56×10^{11}
60	45	78.17	750.85	90	75	2.19×10^6	8.23×10^{11}
60	55	39.55	56.75	90	80	2.61×10^6	1.2×10^{12}
60	65	23.05	11.82	90	85	3.86×10^6	2.33×10^{12}

Table 5-9: Correlations between model and measurement for the Acktar-coated Titanium sharp edge sample, averaged over all scatter angles. The ratios computed are after the conversion factor was applied (see Section 5.3.1). Variance is computed as σ^2 of the ratio over all scatter angles, so values close to zero indicate a stable ratio. In general the model seems to under-predict the measurements, with strong correlations at low sample azimuths and high incidence angles. The breakdown of the correlations at many orientations is thought to be a ray sampling issue.

For all four samples the correlation analysis shows that the model consistently under-predicts the measurements made by TSW. The configurations with the best and most stable correlations are those with $\theta_i > 55°$ and sample azimuths less than 80°. Several factors contribute to the large variances. The first at large azimuth angles is a function of how the source illuminates the edge at these substantial
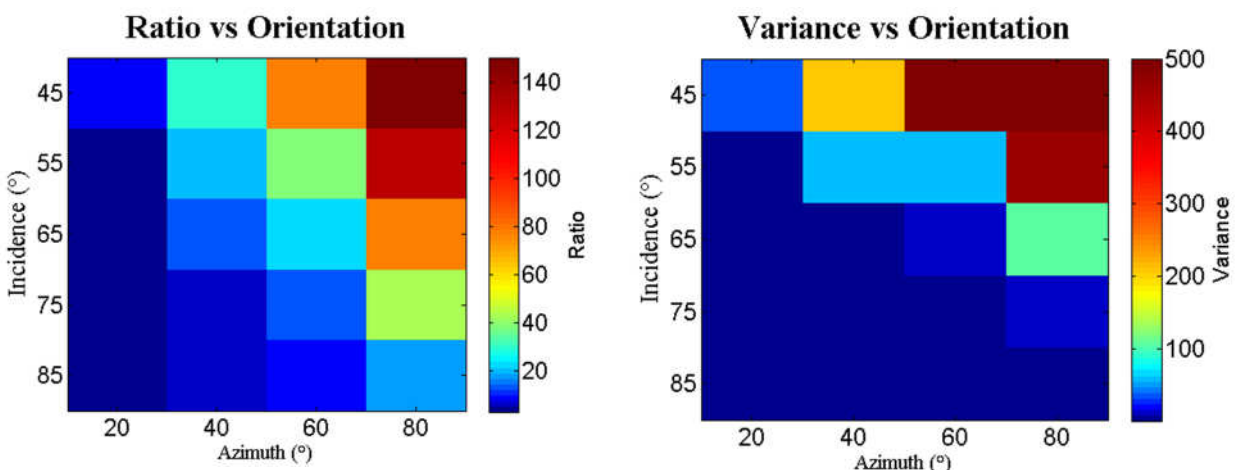

Figure 5-18: A graphical representation of the Ratio and Variance in Table 5-9 for the Acktar Titanium sample showing that the model and measurements are reasonably well correlated at low azimuth and high incidence angles, but virtually uncorrelated with very poor ratios at large azimuths and low incidence angles.

incident angles. The edge length illuminated is quite large so any roughness or variation in the edge shape will be sampled in a single measurement. Also, the accuracy of the assumptions for the conversion from BRDF to scattering fraction may be breaking down for these measurements. Additional exploration of these limits is recommended to understand if the large discrepancy between the model and the measurement is real or just an artifact of both the model and the simulation.

At the moderate azimuth angles, the limitation at low incident angle is likely due to the ray sampling in the model. Given the sharp edge, the necessary scatter angle required for a ray to be collected by the sensor, and the overall geometry, very few of the starting rays get to the collection aperture in the model. This model was not optimized to include importance sampling as was done for the full system model, which led to ray statistics that were very poor at certain orientations. For the well correlated cases, ~10^5 rays were collected for the model. In those cases where the correlation was extremely poor, only ~10^2 rays were collected. Applying the same principles to optimize the model as were applied to the system model is possible, and recommended to be able to resolve the discrepancies due to lack of model detail (as discussed below) and due to poor model statistics. At this time, we believe the primary discrepancy is due to poor model statistics, but a substantial discrepancy remains even where the statistics are good.

In the cases with good statistics, the model appears to under-predict the measurements by factors of 3 to more than 10. As such, it reflects that the system model, while a good geometric model, may be missing some key features which would increase the overall scatter substantially. One obvious possibility is diffraction as included in the JPL model[16]. Their results showed for θ_{az} = 0° the diffraction component was many time that of the scatter. Our data (shown in Figure 4-8) shows that the θ_{az} = 0° measured value is only modestly larger than that of θ_{az} = 20° and following the general trend with increasing θ_{az}. We cannot explain this discrepancy at this time.

Based on our data, one likely large contributor to the higher measured values is some level of edge non-uniformity as shown in Section 4.3.4. This can be due to a variety of effects, including roughness of the edge, difference in the edge RoC along the edge, or differences in coating uniformity along the edge. Depending on future work in fabrication methodologies, this contributor may need to be added to the model, either directly or as a degradation factor to the results. At larger azimuth angles, more of the edge is illuminated by the source so more scatter due to roughness and non-uniformity is likely.

Another potential contributor, but most likely from sample to sample rather than in a single data set, is that we estimated the edge RoC from the SEMs of the corners as we didn't have any way (without destroying the coupons) to measure the RoC that was in the region measured for scatter. If for any reason the edge RoC was actually much larger than the 20 μm used in the model, the measurement would be correspondingly larger. We haven't found any specific reason to distrust the model, but further validation of a model that implemented both a non-ideal edge surface and that provided better ray statistics is important to validate that other physical effects are not coming into play at the extremes of the parameter space explored.

6 CONCLUSIONS

6.1 MILESTONE COMPLIANCE

The 2012 Starshade Stray Light Mitigation through Edge Scatter Modeling and Sharp Edge Materials Development TDEM was awarded to address the milestone:

TDEM Milestone: Develop a scattered light simulation and use it to derive requirements for the edge radius of curvature and scattering properties; build and test at least two sharp edge samples to evaluate the feasibility of flight-compatible materials being fabricated to the derived requirements and how well such a sample performs compared to the predictions of the simulation.

The status of this milestone is as follows:

Four different sharp edge samples were built by NG to evaluate our current capabilities to machine high-precision, black edges. It was found that, while there are certain issues regarding smoothness along the edge, sharp edges with a RoC of 15 – 20 μm can be consistently machined into Aluminum, Titanium, and Beryllium-Copper substrates using standard machining processes, and that the application of various black coatings to such substrates adheres well to the edge without changing its properties. Based on the engineering judgment of our manufacturing team, we believe it is reasonable to assert that a 10 μm RoC for metallic materials is achievable using more complex fabrication processes, at least in some materials. As a proof of concept, this can be done for elements such as razor blades, which have very small RoCs. The challenge is achieving the same small RoC for a much smaller bevel angle, which is likely necessary for safe handling of the edges during ground testing.

A high fidelity scattered light simulation of the starshade flight system (assuming an NWO architecture) was developed by PE, independent of any previous work done attempting to characterize the scatter performance of the starshade edge. The simulation was used to model the performance of six different edge concepts. Four of these six edge concepts were derived from the sharp edge samples manufactured by NG and reflect the machining capabilities demonstrated under this TDEM; the remaining two edge concepts were derived from the NWO ASMCS[4], which proposes a Graphite edge.

The optical performance of each sharp edge coupon machined by NG was measured by TSW in their lab. Subsequently, the TSW lab setup was simulated by PE for each sharp edge coupon in order to provide overlap between the model and experimental results and establish ground truth. After comparison to experiment it was found that our simulation consistently under-predicts the results of the measurements by factors of 3 – 10. The functional behavior of the model and measurements agree well over most orientations, but correlation between the model and experiment breaks down at orientations where ray sampling becomes problematic. Ray sampling is a problem typical to these kinds of simulations. We note that the NWO model was optimized to solve the ray sampling problem but did not do the same kinds of optimization for the test comparison model. Because of this, we have more confidence in the NWO model as a whole, and reasonable confidence in the test comparison model when ray statistics are good, but far less confidence for the test model when statistics are poor.

For each edge concept the outputs of the PE model were used to derive speculative engineering requirements for the starshade edge. Assuming the requirement that at least 2/3 of the circumference of the starshade would be at or below the flux level of a 31st magnitude planet, an edge made of

Titanium, coated with Acktar Magic Black™, would require an edge RoC of approximately 18 μm, according to the model results. However, as we noted above, our stray light model under-predicts the TSW measurements at all orientations. This inconsistency needs to be understood prior to establishing firm requirements to meet the performance objectives of the mission. The disagreement may be a result of differences in the behavior between a sharp edge and a flat surface, potentially due to the large collecting area of the scatterometer when the scatter profile is rapidly changing. Variability in the edge itself is certainly a contributor to the discrepancy, as is the ability to accurately estimate the edge RoC for use in the model comparison.

Via the research characterized in this report and summarized in this section, we have complied with every aspect of the TDEM milestone established at the beginning of this TDEM effort. Additionally, via the steps highlighted in Table 2-1, the advances made under the work of this TDEM provide a strong case for moving the TRL of the starshade edge from 3 to 4.

6.2 STRAY LIGHT ERROR BUDGET

The primary objective of this work is to make progress towards developing requirements for the edge properties of the starshade, in order to achieve the detection of exoplanets, which are technically feasible and that also enable the highest sensitivity possible for a starshade mission. After considering our results, it seems that a reallocation of error terms is in order.

Early NG work provided an error budget that suggested each contributor to the background should be 1/10th that of a notional planet. Minimum planet brightnesses, calculated using the data presented in Turnbull et al[2], show that the faintest habitable zone (HZ) planet around the faintest target star would be ~33rd magnitude. If this is used to set the performance requirement of the starshade edge, the stray light scattering from the edge would have to be on the order of 10^{-22} Watts in the HZ. Based on the results of our measurements and models, this seems to be a rather daunting prospect, assuming that the systems with 33rd magnitude planets will have HZ's very close to the IWA of the starshade.

There are many reasons to relax the stray light requirement put forth in the NG error budget. It is clear from our simulation that the scattered light distribution is not at all uniform around the starshade edge. The region of the starshade opposite the sun will have a much lower background about the minimum IWA, a quality shared by many other direct imaging methods. Though ideally the dimmest planets expected would be detectable at tight IWA's about the entire circumference of the starshade, reducing the requirement to fractional detectability for these system extremes (closest in, dimmest possible planets) could aid the design process without sacrificing much in the expected mission yields. This would complicate observation planning to ensure sampling of the HZ of various stars, but these are challenges that have been addressed for other approaches. For the vast majority of the target stars, the expected minimum detectable Earth-like planet in the HZ will be at least 1, if not 2 orders of magnitude brighter than the 33rd magnitude planets being discussed. Also worth noting is that the scattered sunlight is constant for all targets (as a function of starshade angle to the sun), while all other stray light terms are dependent on the brightness of the host star and the amount of stellar PSF leakage around the starshade. Fainter targets will thus tend to have reduced stray light from other contributors, which should make a less stringent scattered sunlight requirement feasible without significantly impacting the overall observations.

Further analysis of our data is clearly needed in order to better establish the influence of the stray light performance modeled on planet detectability. We must further investigate the background levels at which a planet is no longer detectable, the dependence that detectability has on IWA, and the extent to which reducing the stray light requirements on the starshade edge will affect overall mission performance. Processing methods, including the subtraction of the edge scatter signal from images, which would leave only the residual noise increase in the area, are worth considering as a possibility for reducing the scatter effects of the starshade edge on detectability.

6.3 FUTURE WORK

Prior to and during this TDEM, NG has developed the equipment and team necessary to carry out future work regarding the starshade edge. The experience of the team can be utilized in the future endeavors of the field. Direct follow-on work that stems from this TDEM include:

- Complete the current effort to incorporate the stray light distribution function into an image simulation to determine the effective IWA around the starshade image as a function of planet, star, and exo-zodiacal light brightness. Insights gained from current and future analysis could be used to reallocate the stray light error budget.
- Further investigate the differences between the simulations developed independently by PE, NG, and JPL, including all architecture differences and apply the modeling of the diffraction component developed by JPL to our simulation results. This would include understanding the relevant scaling factors in order to apply our results to different mission architectures (like WFIRST), and the derivation of edge design requirements for a variety of mission designs.
- Expand the current work to include samples of more edge designs of interest, such as Carbon NanoTubes and Graphite. The high performance of Graphite (a specular surface) shown in this study relative to the other samples (diffuse surfaces) suggests that we need to evaluate many new edge concepts moving forward. A further look into various sharp edge manufacturing techniques to improve our minimum RoC and edge uniformity capabilities is also desirable. It would be beneficial to learn our current limits regarding the fabrication of sharp edges, which processes are compatible with the construction of a precision shaped edge, and which candidate materials meet the more stringent flexibility requirements of the Exo-S deployment scheme.
- Investigate the causes of the lack of correlation between our simulation and measurements at high azimuth and lower incidence angles. The key elements are likely optimization of the ray trace approach to eliminate the ray sampling issues and a way to estimate the edge roughness.

7 REFERENCES

Additional information on FRED is available here: http://photonengr.com/software/

Additional information on Enbio's coatings is available here: http://www.enbio.eu/

Additional information on Acktar's coatings is available here: http://www.acktar.com/

Additional information on TSW's CASI scatterometer is available here: http://thescatterworks.com/scatterometers/casi

1 NRC Astronomy and Astrophysics Survey Committee, New Worlds, New Horizons in Astronomy and Astrophysics, The National Academies Press, Washington, DC, 2010.

2 Turnbull, M., Glassman, T., Roberge, A., Cash, W., Noecker, C., Lo, A., Mason, B., Oakley, P., Bally, J., "The Search for Habitable Worlds: 1. The Viability of a Starshade Mission", Publications of the Astronomical Society of the Pacific, 124, 418, 2012.

3 Siegler, N., "Exoplanet Exploration Program Technology Plan Appendix", Jet Propulsion Laboratory Publications, Pasadena, CA, 2016.

4 Cash, W., et al. "The New Worlds Observer: the Astrophysics Strategic Mission Concept Study", 2009, Proc. SPIE, 7436, 5

5 Lo, A., Glassman, T., Daily, D., Casement, S., Marks, G., "Technology Development for the Starshade to Enable High Contrast Imaging", in IEEE Aerospace Conference, 6187185, 2012.

6 Casement, S., Cash, W., Glassman, T., Warwick, S. "Starshade Stray Light Mitigation through Edge Scatter Modeling and Sharp-Edge Development", NASA Proposal Number 12-SAT12-0040, 2013.

7 Arenberg, J., Glassman, T., Lo, A. "Effects of Scattered Light on the Performance of the New Worlds Starshade", in Proc. of SPIE, Vol. 6693, 1E, 2007.

8 Casement, S., Flannery, M., Glassman, T., Lo, A. "Starshade Design Driven by Scattered Light from Edge Scatter", in Proc. of SPIE, Vol. 8442, 4H, 2012.

9 Casement, S., Cash, W., Glassman, T., Warwick, S. "Starshade Stray Light Mitigation through Edge Scatter and Sharp-Edge Materials Development", JPL Document D-94003, 2014.

10 *Solarblack Data Sheet*. 1st ed. Dublin: N.p., 2016. Web. 2 Feb. 2016. http://www.enbio.eu/Portals/0/downloads/SolarBlack.pdf

11 Landini, F., Romoli, M., Vives, S., Baccani, C., Escolle, C., Pancrazzi, M., Focardi, M., Da Deppo, V., Moses, J., Fineschi, S., "Coating and Surface Finishing Definition for the Solar Orbiter/METIS Inverted External Occulter", in Proc. of SPIE, Vol. 9151, 91515H-15.

12 Salomon, Y., Sternberg, N., Gouzman, I., Lemperr, G., Grossman, E., Katsir, D., Cotostiano, R., Minton, T., "Qualification of Acktar TM Black Coatings for Space Application", http://esmat.esa.int/materials_news/isme09/pdf/4-New/S7%20-%20Miron-Salomon.pdf

13 Seager, S. and the STDT, "Exo-S: Starshade Probe-Class Exoplanet Direct Imaging Mission Concept Final Report," NASA JPL Document CL #15-1155, March 2015.

14 Salomon, Y.M., Sternberg, N.A., Gouzman, I., Lempert, G., Grossman, E., Katsir, D., Cotostiano, R., "Qualification of Acktar™ Black Coatings for Space Application," 11th ISMSE, Aix-en-Provence, France, 2009.

15 Stover, John C., "Measuring and Quantifying Scatter from a Variety of Sample Types", in Proc. Of SPIE Vol. 9628, 96280K-1.

16 Martin, Stefan R., Shaklan, S., Crawford, S., Lee, S-C., Khayatian, B., Hoppe, D., Cady, E., Lisman, P.D., "Starshade Optical Edge Modeling, Requirements and Laboratory Tests," in Proc. of SPIE Vol. 8864, 88641A-1.